

"Influence of the plasma chemistry and energetics of an Al cathodic arc discharge on the composition and structure of Alumina thin films"

Von der Fakultät für Georessourcen und Materialtechnik
der Rheinisch-Westfälischen Technischen Hochschule Aachen

zur Erlangung des akademischen Grades eines

on and similar papers at core.ac.uk

genehmigte Dissertation

provided by Publikationss

vorgelegt von **M.Sc.**

Adil Atiser

aus Ankara

Berichter: Univ.-Prof. Jochen M. Schneider, Ph.D.
Univ.-Prof. Dr.rer.nat. Joachim Mayer

Tag der mündlichen Prüfung: 25. März 2010

Diese Dissertation ist auf den Internetseiten der Hochschulbibliothek online verfügbar.

Materials Chemistry Dissertation

No.: 10 (2011)

Adil Atiser

**Influence of the plasma chemistry and energetics of
an Al cathodic arc discharge on the composition and
structure of Alumina thin films**

Shaker Verlag
Aachen 2011

Bibliographic information published by the Deutsche Nationalbibliothek

The Deutsche Nationalbibliothek lists this publication in the Deutsche Nationalbibliografie; detailed bibliographic data are available in the Internet at <http://dnb.d-nb.de>.

Zugl.: D 82 (Diss. RWTH Aachen University, 2010)

Copyright Shaker Verlag 2011

All rights reserved. No part of this publication may be reproduced, stored in a retrieval system, or transmitted, in any form or by any means, electronic, mechanical, photocopying, recording or otherwise, without the prior permission of the publishers.

Printed in Germany.

ISBN 978-3-8322-9842-5

ISSN 1861-0595

Shaker Verlag GmbH • P.O. BOX 101818 • D-52018 Aachen

Phone: 0049/2407/9596-0 • Telefax: 0049/2407/9596-9

Internet: www.shaker.de • e-mail: info@shaker.de

Abstract

In this thesis the relationship between plasma chemistry and energetics and thin film properties was investigated for an Al cathodic arc discharge. A virtually monoenergetic beam of single charged Al ions was generated at pressure distance products higher than 128 Pa.cm. In the literature Al cathodic arc discharges always contained a high energy tail which made it difficult to analyse the influence of plasma parameters on thin film properties. Thermalization of the cathodic arc discharge is expected at high pressure distance products. What made this work particularly interesting is that the thermalization effect was observed at conditions where the deposition rates were still high (about 1nm/s). It was shown that crystalline films containing α - and γ -Al₂O₃ phases could be grown using cathodic arc discharges containing monoenergetic single charged Al ions. This is a prerequisite for a meaningful study of the influence of plasma parameters (such as ion flux and energy) on film formation and properties.

The plasma chemistry and energetics of an Al cathodic arc discharge was studied as a function of the filter current. At filter currents < 15 A, the plasma consisted predominantly of Al⁺ ions (>94%). At filter currents > 17 A Ar and oxygen ion populations increase and dominate the plasma composition. The average energy of the Al⁺ ions does not vary significantly. The total as well as Al⁺ ion flux, however, decreases for one order of magnitude as the filter current is increased from 10 to 20 A. According to XRD and SAED data, the films grown at 10, 17, and 20 A are γ -Al₂O₃. The films grown at 12 and 15 A contain a phase mixture of α -Al₂O₃ and γ -Al₂O₃. The α -Al₂O₃ phase may have been formed due to additional energy that was added to the substrate via higher ion flux. At 10 A the film thickness was about

200nm which corresponds to earlier reports suggesting that $\alpha\text{-Al}_2\text{O}_3$ formation succeeds a thin $\gamma\text{-Al}_2\text{O}_3$ film of about 200 nm. The grain size was calculated to be in the range from 20 to 30 nm. The average Young's modulus values of $\gamma\text{-Al}_2\text{O}_3$ films were 7-20% lower than literature values. SEM and TEM investigations show that dense films can be deposited with columnar as well as equiaxed grains.

Thin films were deposited at substrate bias potentials ranging from -8 V to -300 V on TiAlN coated Si wafers at a filter current of 20 A. All films exhibited an O/Al ratio of $1.5 \pm 1\%$ and are hence close to stoichiometric alumina. XRD data indicate the formation of $\gamma\text{-Al}_2\text{O}_3$ in all films. There was no evidence for the presence of other phases. The Young's modulus values of the films grown from -50 to -250 V deviated up to 14% from the Young's modulus values of $\gamma\text{-Al}_2\text{O}_3$ from literature (350 Gpa). It is found that the films grown from -50 to -250 V are dense with equiaxed grains. TEM analysis of films grown at -200 V show dense, phase pure $\gamma\text{-Al}_2\text{O}_3$ with equiaxed grains of about 20 nm size. The application temperature of $\gamma\text{-Al}_2\text{O}_3$ coated cutting inserts containing a TiAlN interlayer is limited to temperatures below 1000°C based on our annealing experiments in air.

Zusammenfassung

In dieser Arbeit wurde die Beziehung zwischen Plasmachemie und Energetik und den Dünnschicht-Eigenschaften für eine kathodische Bogenentladung mit Al-Ionen untersucht. Ein nahezu monoenergetischer Strahl von mono-geladenen Al-Ionen wurde bei einem Druck-Entfernungs Produkt über 128 Pa.cm generiert. In der Literatur beschriebene kathodische Bogenentladung-Verteilungen für Al-Ionen zeigen immer relativ hohe Energiewerte im Endbereich der Verteilung, der es schwierig machte, den Einfluss der Plasma-Parameter auf die Dünnschicht-Eigenschaften zu analysieren. Die Thermalisierung der kathodischen Bogenentladung ist ein erwartetes Ergebnis bei hohen Druck-Entfernung-Produkten. Dieser Arbeit ist besonders interessant, weil die Thermalisierung unter Bedingungen beobachtet wurde, bei denen die Abscheiderate noch sehr hoch (ca. 1 nm / s) war. Es wurde gezeigt, dass kristalline Schichten mit α - und γ - Al_2O_3 -Phasen abgeschieden werden konnten mit monoenergetischen mono-geladenen Al-Ionen aus kathodischen Bogenentladungen. Dieses Ergebnis erlaubt eine einfachere Untersuchung des Einflusses der Plasma-Parameter (z. B. Ionenfluss und Energie) auf die Dünnschicht-Eigenschaften.

Die Plasma-Chemie und die Energetik einer Al-kathodischen Bogenentladung wurden als Funktion des Filterstroms untersucht. Bei Filterströmen $<15\text{A}$ bestand das Plasma vorwiegend aus Al^+ -Ionen ($>94\%$). Bei Filterströmen $>17\text{A}$ erhöht sich die Ar- und O_2 -Ionen-Population und dominiert die Plasma-Zusammensetzung. Die durchschnittliche Energie der Al^+ -Ionen weichen nicht wesentlich von einander ab. Der Total- sowie Al^+ -Fluss nimmt jedoch um eine Größenordnung zu, wenn der Filterstrom von 10 auf 20 A erhöht wird. XRD- und SAED- Ergebnisse zeigen, dass die

bei 10, 17 und 20 A abgeschiedenen Filme $\gamma\text{-Al}_2\text{O}_3$ enthalten. Die bei 12 und 15 A abgeschiedenen Filmen enthalten eine Phasenmischung aus $\alpha\text{-Al}_2\text{O}_3$ und $\gamma\text{-Al}_2\text{O}_3$. Die $\alpha\text{-Al}_2\text{O}_3$ -Phase könnte durch die zusätzliche Energie, die auf das Substrat durch höheren Ionenfluss gebracht wurde, entstanden sein. Die Korngröße wurde zu 20 - 30 nm berechnet. Der durchschnittliche E-Modul Wert der $\gamma\text{-Al}_2\text{O}_3$ Filme wurde 7-20% niedriger als die Werte in der Literatur gemessen. SEM- und TEM-Untersuchungen zeigen, dass dichte Filme mit säulenförmigen sowie gleichachsigen Körnern aufgebaut werden können.

Dünne Filme wurden bei Substrat-Bias-Potenzialen von -8 V bis -300 V auf TiAlN beschichteten Si-Wafern bei einem Filterstrom von 20 A abgeschieden. Alle Filme zeigten ein O/Al-Verhältnis von $1,5\pm 1\%$ und sind damit in der Nähe von stöchiometrischem Aluminiumoxid. XRD-Ergebnisse zeigen die Bildung von $\gamma\text{-Al}_2\text{O}_3$ in allen Filmen. Es gab keine Hinweise auf das Vorhandensein von anderen Phasen. Der E-Modul Werte der von -50 bis -250 V abgeschiedenen Filme weichen bis zu 14% von den Young's-Modulus-Werten von $\gamma\text{-Al}_2\text{O}_3$ aus der Literatur (350 GPa) ab. Die bei -50 V bis -250 V abgeschiedenen Filme sind dicht. Das TEM-Bild für den bei -200 V abgeschiedenem Film zeigt eine dichte $\gamma\text{-Al}_2\text{O}_3$ -Schicht mit Körnern von etwa 20 nm Größe. Aufgrund von Glüh-Experimenten in Luft ist die Einsatztemperatur von $\gamma\text{-Al}_2\text{O}_3$ beschichteten Wendeschneidplatten mit einer TiAlN-Zwischenschicht auf Temperaturen unterhalb 1000 ° C begrenzt.

Preface

The work presented here is a summary of research performed at Materials Chemistry, RWTH Aachen University.

Publications

Papers contributing to this thesis

Paper I **Pressure dependence of the Al ion energy distribution functions during filtered cathodic arc thin film growth in an Ar, O₂ ambient**

A. Atiser, S. Mráz and J. M. Schneider

J. Phys. D: Appl. Phys. **42** (2009) 015202 (6pp)

Papers not contributing to this thesis

Paper II Synthesis and characterization of boron–oxygen–hydrogen thin films at low temperatures

Denis Music, H. Kölpin, A. Atiser, U. Kreissig, T. Bobek, B. Hadam, J. M. Schneider

Materials Research Bulletin 40 (2005) 1345–1352

Paper III Influence of argon and oxygen on charge-state-resolved ion energy distributions of filtered aluminum arcs

J. Rosén, A. Anders, S. Mráz, A. Atiser, and J. M. Schneider

Journal of Applied Physics **99**, 123303 (2006)

Paper IV Thermal residual stress analysis in continuous Al₂O₃ fiber reinforced NiAl composites

H. Chen, W. Hu, A. Atiser, Y. Zhong, G. Gottstein

Int. J. Mat. Res. (formerly Z. Metallkd.) 97 (2006) 1320-1327

Acknowledgements

My wife, Randi, for being supportive of me and believing in me.

To my daughters, Bilge and Gönül, they are the best product of the Ph.D. years.

My mother and father.

To all my colleagues. I will cherish my memories with you.

Academical thanks go to three people:

Special thanks go to Stano who was always there when I needed him,
provided that it is after 17:00.

To Johanna as her work laid the framework of mine.

To Jochen: for the opportunity and guidance.

The author acknowledges the financial support granted by the Deutsche
Forschungsgemeinschaft (DFG) within the project Schn 735/14.

Contents

Abstract	v
Zusammenfassung	vii
List of publications	ix
Acknowledgements	xi
1. Introduction	1
2. Alumina	5
3. Experimental setup and deposition technique	10
3.1 Experimental setup	10
3.1.1 The Vacuum Chamber	10
3.1.2 The Source	12
3.1.3 The Substrate Holder	12
3.2 The Deposition Technique	12
3.2.1 Plasma generation	13
3.2.2 The ion transfer	15
3.2.3 The sheath	16
4. Characterization techniques	18
4.1 Plasma characterization	18
4.1.1 Mass spectrometry	18
4.1.1.1 Extraction orifice	19
4.1.1.2 Optical ion transfer system	19

4.1.1.3	Energy filter	19
4.1.1.4	Mass filter	20
4.1.1.5	Secondary electron multiplier	20
4.1.2	Langmuir probe	20
4.2	Film characterization	21
4.2.1	Chemical composition analysis	21
4.2.2	Structural analysis	22
4.2.3	Morphology and microstructure	23
4.2.4	Mechanical property analysis	25
5.	Results and Discussion	29
5.1	Pressure dependence of the Al ion energy distribution functions during filtered cathodic arc thin film growth in an Ar, O ₂ ambient	29
5.2	Influence of plasma chemistry and ion flux on phase formation and deposition rate of Al ₂ O ₃ films grown with cathodic arc	42
5.3	Influence of substrate bias potential on phase formation and elastic properties of Al ₂ O ₃ films grown with cathodic arc	58
6.	Conclusions and Future Work	73
6.1	Conclusions	73
6.2	Future Work	76

1. Introduction

Materials Science is a field of science which studies the properties of materials and their potential applications in daily life. Thin film research has developed as a branch of this broad field in order to further enhance and control the properties of materials and their use. Thin films are in great use today with an emerging market, in fields such as electronics, optics, and mechanics among others. Thin films enhance the properties of the substrate that they are deposited on and enable what was not achievable before in terms of properties. With scientists, engineers, and investors working further in this field, it is inevitable that more and more applications of coatings will be seen in near future.

As Milton Ohring¹ states, thin film technology is one of the oldest arts and one of the newest sciences simultaneously. The history of thin films dates back to 1500 B.C. when Egyptians were able to produce gold leaf samples of 300nm thickness. One of the most common deposition techniques today, magnetron sputtering, has developed significantly in the last century.²

Thin films are essentially thin layers of a material that is deposited on a surface. They can be created by various processes which apply different physical principles in order to achieve the demanded properties for the application in question. Vapor phase depositions are grouped into two types of processes: CVD, Chemical Vapor Deposition, and PVD, Physical Vapor Deposition. In CVD there are reactions in the gas phase as well as on the deposition surface, whereas in PVD reactions only occur on the surface. CVD processes are generally thermal processes where the process temperature is kept relatively high. One

way to improve the process and to decrease the process temperature is to ionize a part of the gas phase. In this case, the process is called PECVD, Plasma Enhanced Chemical Vapor Deposition. Within PVD there are few processes which differ significantly from each other with respect to the physics underlying these processes. The most simple process would be evaporation or sublimation of a liquid or solid target. The gas formed would deposit on the surface of the substrate to form a thin film. In order to decrease the substrate temperature as well as to activate surface diffusion at lower temperatures, plasma assisted processes are employed, where the plasma adds further energy to the surface of the growing film. Magnetron sputtering is one of the most common plasma assisted PVD methods. The particles are sputtered from a target with the help of ionized gas particles (Ar^+ etc.). The particles that are sputtered can be neutral as well as ionized. The ionization fraction of the sputtered species is usually of the order of a few percent and the majority of charged particles extracted to the substrate are ions of the sputtering gas.³ The vacuum arc is a low voltage, high current plasma discharge that takes place between two electrodes in vacuum with an ionization fraction up to 100%.^{4,5} This high degree of ionization and the higher deposition rates make the cathodic arc process very interesting for industrial application. This process will be further discussed in the third chapter. For further information on these methods the reader may refer to the following literature.^{1,2,6,7}

Aluminum oxide, also known as alumina, is the oxide of aluminum and has the chemical formula Al_2O_3 . Alumina exists in various structural polymorphs,

which are stable over a wide range of temperatures. Besides the most stable α -alumina (corundum, sapphire) there exists a variety of so-called transition phases ($\eta, \gamma, \theta, \delta$).⁸ Alumina coatings are known to exhibit advantageous mechanical properties as well as chemical inertness and oxidation resistance at high temperatures.⁹ It is also known to be highly insulating and optically transparent.¹⁰

In order to control the phase formation of alumina thin films deposited by the filtered cathodic arc (FCA) deposition process, there exists a variety of parameters to optimize. It has already been mentioned that the substrate temperature is important. The major restriction to this parameter comes from the possible phase transformation, grain growth, and other property changing mechanisms occurring at the substrate at elevated temperatures. In order to avoid this, the plasma supplies energy to the near surface area, while the bulk of the substrate remains cooler, sustaining its structure and properties.

The chemistry and energetics of the plasma which supplies the additional energy to the surface are therefore major parameters affecting the phase formation and growth morphology of the growing thin film. This thesis is written in order to contribute towards understanding the correlation between plasma chemistry, energetic, and flux on the phase formation and growth morphology of alumina thin films deposited by FCA.

-
- ¹ M. Ohring, *The Materials Science of Thin Films : Deposition and Structure* (Academic Press, 1992) (xix,xx)
 - ² W. D. Westwood, *Sputter Deposition* (AVS, New York 2003) (ix-x)
 - ³ J. Alami, J. T. Gudmundsson, J. Bohlmark, J. Birch and U. Helmersson, *Plasma Sources Sci. Technol.* 14 525-531 (2005)
 - ⁴ B. K. Tay, Z. W. Zhao and D. H. C. Chua, *Material Science and Engineering R* 52 1-48 (2006)
 - ⁵ A. Bendavid, P. J. Martin, X. Wang, M. Wittling and T. J. Kinder, *J. Vac. Sci. Technol. A* 13(3) 1658-1664 (1995)
 - ⁶ D. L. Smith, *Thin Film Deposition, Principles and Practice* (McGraw-Hill Inc. 1995)
 - ⁷ A. Anders, *Handbook of Plasma Immersion, Ion Implantation and Deposition*, (John Wiley & Sons, Inc. 2000)
 - ⁸ Z. Lodziana, K. Parlinski, *Physical Review B* 67,174106 (2003)
 - ⁹ O. Kyrlyov, D. Kurapov, J. M. Schneider, *Appl. Phys. A* 80, 1657-1660 (2005)
 - ¹⁰ J. M. Andersson, Z. Czigan, P. Jin, U. Helmersson, *J. Vac. Sci. Technol. A* 22(1) 117-121 (2004)

2. Alumina

Alumina exhibits a high compression strength¹ (3,861 GPa) and high hardness² (20 GPa) as well as good wear and corrosion properties.³ The thermal conductivity of alumina is relatively high with respect to ceramics, which explains its good thermal shock resistance.⁴ For thin films ranging from 10 to 200 nm, the dielectric strength of alumina was found to be up to 1.36×10^7 V/cm.⁵ As of June 2009, a search in sciencedirect.com results in more than 160.000 publications, when the word “alumina” is entered.

However, these properties are measured for the thermodynamically stable phase of alumina, the alpha phase: $\alpha\text{-Al}_2\text{O}_3$. Besides $\alpha\text{-Al}_2\text{O}_3$, there are numerous phases including the η , χ , κ , γ , δ and θ phases.⁶ These phases have significantly different properties, for example the density of the $\gamma\text{-Al}_2\text{O}_3$ phase is about $3,6 \text{ g/cm}^3$, while the density of the $\alpha\text{-Al}_2\text{O}_3$ phase is about $3,9 \text{ g/cm}^3$. $\gamma\text{-Al}_2\text{O}_3$ was shown to be thermodynamically stable at specific surface areas larger than $125 \text{ m}^2/\text{g}$ due to its lower surface energy.⁷ Mechanical properties of these two phases, which are frequently seen particularly in thin film growth via physical vapor deposition, are also significantly different. The Young's modulus value of $\alpha\text{-Al}_2\text{O}_3$ was measured by Oliver and Pharr to be around 440 GPa.⁸ The Young's modulus of $\gamma\text{-Al}_2\text{O}_3$ calculated from bulk modulus values reported by ab-initio calculations⁹ and experimental measurements¹⁰ agree with each other and are around 350 GPa. In Figure 2.2, the unit cells of $\alpha\text{-Al}_2\text{O}_3$ and $\gamma\text{-Al}_2\text{O}_3$ phases are presented. The space group of $\alpha\text{-Al}_2\text{O}_3$ is $r\bar{3}c$ which corresponds to a rhombohedral structure. The structure of $\gamma\text{-Al}_2\text{O}_3$ is still

under debate, often a defect cubic spinel with space group $fd\bar{3}m$ is used in discussions.

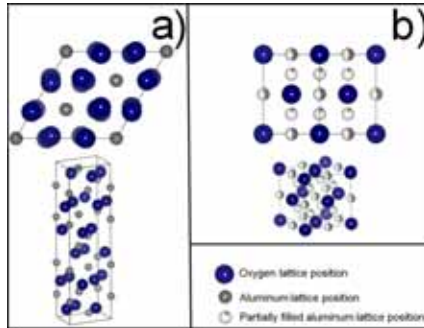


Figure 2.2: Unit cells for a) α - Al_2O_3 (rhombohedral, $r\bar{3}c$) and b) γ - Al_2O_3 (defect cubic spinel, $fd\bar{3}m$) (Calculated atomic positions, courtesy of Thomas Reeswinkel)

Crystalline Al_2O_3 thin films are of interest to the industrial and scientific community due to their applicability in fields ranging from corrosion,¹¹ catalytic support,¹² diffusion barrier,¹³ and wear protection¹⁴ to microelectronics.¹⁵ The most established synthesis method of alumina films is CVD (Chemical Vapor Deposition),¹⁶ where the substrate temperature is typically well above 1000°C. Decreasing the substrate temperature has been a major goal for alumina (in particular α - Al_2O_3) synthesis as most technologically relevant substrate materials undergo property changes at elevated temperatures. Hence, alternative routes were investigated to deposit alumina phases. γ - Al_2O_3 thin films were deposited by plasma enhanced chemical vapor deposition at temperatures of 500-600°C.¹⁷ Chromia templates or initially oxidized CrN substrates were used to enable α - Al_2O_3 phase formation at lower temperatures such as 400°C¹⁸ and 700°C¹⁹, where Cr_2O_3 is acting

as a seed layer for α - Al_2O_3 . Zywitzki et al. have used plasma activated electron beam evaporation for growing high quality dense γ - Al_2O_3 films at 700°C .²⁰ Ionized magnetron sputtering was used to deposit low temperature crystalline alumina including κ - Al_2O_3 at temperatures as low as 320°C .²¹ Using cathodic arc deposition thin films containing γ - Al_2O_3 and α - Al_2O_3 phases were deposited at temperatures as low as 600°C .²² Recently, high power impulse magnetron sputtering was used to deposit films containing the α - Al_2O_3 phase at 575°C .²³

-
- ¹ Ryshkewitch, E., Ber. Dtsch. Keram. Ges., **22**: p. 54 (1941)
- ² M. Sridharan, M. Sillassen, J. Bøttiger, J. Chevallier, H. Birkedal, Surf. & Coat. Tech. **202**, 920-924 (2007)
- ³ Muenstermann S., Telle R., *Wear* (2008), doi:10.1016/j.wear.2009.06.014
- ⁴ Gitzen, W. H., Alumina as a Ceramic Material, The American Ceramic Society 58-59 (1970)
- ⁵ Kawamura, H., Azuma K., Journal of the Physical Society of Japan, Volume 8, Issue 6, pp. 797 (1953)
- ⁶ G. Paglia, A. L. Rohl, C. E. Buckley, J. D. Gale, Physical Review B **71**, 224115_2005_
- ⁷ J. M. McHale, A. Auroux, A. J. Perrotta, A. Navrotsky, Science, 277, 788 (1997)
- ⁸ W. C. Oliver, G. M. Pharr, J. Mater. Res., **7**, 6, 1564 (1992)
- ⁹ G. Gutiérrez, A. Taga, B. Johansson, Phys. Rev. B **65** 012101 (2001)
- ¹⁰ A. Schuetze, D. T. Quinto, Surf. Coat. Technol. **162**, 174 (2003)
- ¹¹ V.A.C. Haanappel, H.D. van Corbach, T. Fransen, P.J. Gellings, Surf. & Coat. Technol. **72**, 13 (1995)
- ¹² C. R. Henry, Surf. Sci. Rep. **31**, 231 (1998)
- ¹³ J. Mueller, D. Neuschuetz, Vacuum **71**, 247 (2003)
- ¹⁴ D. Kurapov, J. Reiss, D. H. Trinh, L. Hultman, J. M. Schneider, J. Vac. Sci. Technol. A **25**, 4, 831 (2007)
- ¹⁵ S. Y. Wu, M. Hong, A. R. Kortan, J. Kwo, J. P. Mannaerts, W. C. Lee, Y. L. Huang, App. Phys. Lett. **87**, 091908 (2005)
- ¹⁶ A.R. Barron, Insulating materials: W.S. Rees Jr. (Ed.), CVD of Nonmetals, VCH, Weinheim, 262-313, 1996.
- ¹⁷ O. Kyrilov, D. Kurapov, J. M. Schneider, Applied Physics A **80**, 8, 1657 (2005)
- ¹⁸ P. Jin, G. Xu, M. Tazawa, K. Yoshimura, D. Music, J. Alami, U. Helmersson, J. Vac. Sci. Technol. A **20** (6) 2134-2136 (2002)
- ¹⁹ T. Kohara, H. Tamagaki, Y Ikari, H. Fujii, Surf. Coat. Technol. **185**, 166 (2004)
- ²⁰ O. Zywitzki, K. Goedicke, H. Morgner, Surf. Coat. Technol. **151-152**, 14 (2002)
- ²¹ J. M. Schneider, W. D. Sproul, A. Matthews, Surf. Coat. Technol. **98**, 1/3, 1473 (1998)

²² R. Brill, F. Koch, J. Mazurelle, D. Levchuk, M. Balden, Y. Yamada-Takamura, H. Maier, and H. Bolt, *Surf. Coat. Technol.* **174–175**, 606 (2003)

²³ E. Wallin, T. I. Selinder, M. Elfving, U. Helmersson, *Europhys. Lett.* **82**, 36002 (2008)

3. Experimental Setup and Deposition Technique

In this chapter the experimental setup will be introduced in detail, including the arc source, the off-plane double bend filter, and the substrate holder. In addition to that an introduction to the deposition technique investigated here will be provided, from the creation of the plasma to its transport and finally the deposition on the samples.

3.1 Experimental Setup

A sketch of the experimental setup, the design, and the construction of which is done by the author of this thesis, is provided in Figure 3.1. The setup can be simplified in 3 elements:

- The Vacuum Chamber: Pumps, pressure gauges, gas feeding, cooling
- The Source: The arc source and the off-plane double bend filter
- The Substrate Holder/The Mass Energy Analyzer

3.1.1 The Vacuum Chamber

The system was evacuated by a turbomolecular pump (Leybold TW-701) attached to a dry piston pump (Leybold Ecodry-M15). The system is first evacuated to pressures below 10 Pa with the dry piston pump, after that the turbomolecular pump is switched on. The base pressure was 10^{-4} Pa for all measurements reported in this thesis. There are three pressure gauges in the deposition system: two convection enhanced pirani gauges and the ion gauge (all Granville Phillips). One of the pirani gauges is installed between the turbomolecular pump and the forevacuum pump. The other pirani gauge and the ion gauge are installed at the bottom of the deposition chamber next to the gas inlet. (Figure 3.1) The pressure for the

measurements was set using only the ion gauge for all measurements executed as a part of this thesis.

The Ar and O₂ gases were fed to the system from the bottom of the chamber with the help of 2 mass flow controllers. Both gases had a purity of 99.999%. The system was vented with N₂ gas with a purity of 99.999%. The transport from gas bottles to the mass flow controller is made by stainless steel tubes which were checked for leaks prior to use.

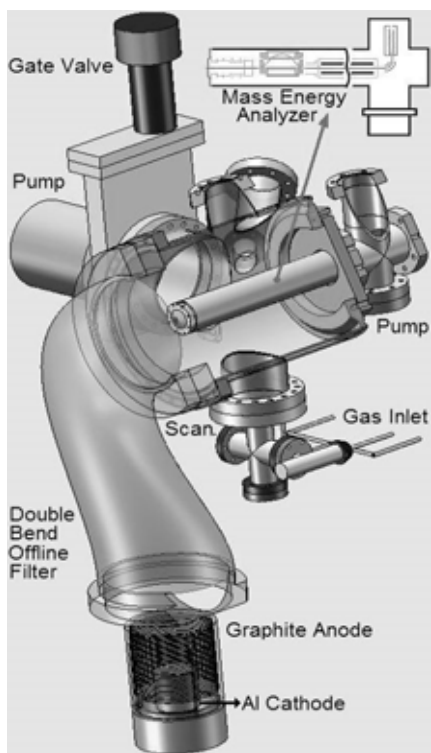


Figure 3.1: Schematic of the experimental setup

3.1.2 The Source

An industrial cathodic arc source (Nanofilm-Singapore) with a double bend off-plane filter and a scanner was employed as the plasma source. Aluminium cathodes with a diameter of 70 mm and purity of 99.5% were used. The anode material was graphite. The graphite anode of the original design has been changed by the author for longer deposition times without breaking the plasma. The plasma scanning matrix (6-6), scanning interval (10 μ s), arc current (110 A), and anode coil current (9 A) were kept constant for all experiments reported here. The only parameter changed on the source side was the filter coil current which will be discussed later in chapter 5.

3.1.3 The Substrate Holder

The substrate holder used in this experiment was capable of heating the sample (Si Wafer) to 700°C using a BN ceramic heater and keeping this temperature constant during growth. The deposition temperature was kept constant (700°C) for all experiments the results of which are reported as a part of this thesis. The maximum potential applied to the sample in this work was -300 V at 100 kHz frequency. A mass energy analyzer was installed exactly at the same position as the sample holder. The details of the mass energy analyzer will be discussed in detail in chapter 4.

3.2 The Deposition Technique

The first experiments which are related to arc discharges date back to 18th century. Priestley reported cathode spots in 1775.^{1,2} Anders reports that Petrov and Davy made, observed and described the first continuous arc discharges independently.³ In the 1960s, modern research on cathodic arc discharges was initiated in the Soviet Union. According to Anders, the history of broad application of

cathodic arc deposition is closely related to work done in the 1960s by a group of researchers at the National Science Center, Kharkov Institute of Physics and Technology (NSC KIPT).⁴ For a through review of the history of cathodic arcs, the book⁴, recently published by Anders, is suggested.

The deposition technique can be simplified into three elements.

- Plasma Generation
- Ion Transfer/Off-plane Double Bend Filter
- Sheath/Deposition on Sample

3.2.1 Plasma Generation

The arc source consists of a cathode and an anode. The cathode is connected to a power generator which sustains high currents and low potentials. The anode is often grounded. The cathodic arc discharge can thus be described as a low voltage - high current plasma between the two electrodes. When this is done in vacuum, it is called a vacuum cathodic arc discharge. In Figure 3.2 the arc source used here as well as a basic drawing of plasma generation is presented. An arc spot, having a radius of 1 to 100 μm , is a source of electrons, metal ions, metal vapor, and macroparticles.⁵ The electron density of a cathodic arc is in the order of 10^{13} to 10^{20} depending on the conditions applied. This is much higher than in other deposition processes, such as sputtering.^{6,7} This high electron density enables further ionization of the neutrals that are present in the system. This in turn yields a very high ion current of up to 10^{12} A/m^2 .⁷

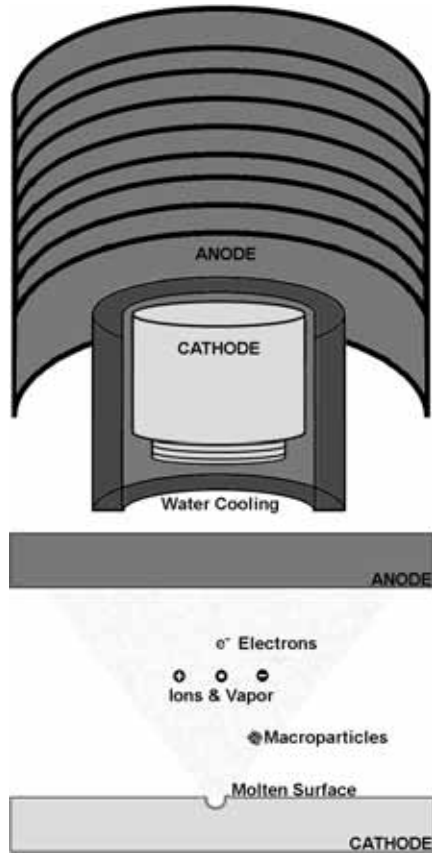


Figure 3.2: The arc source and the plasma generation

In Figure 3.2 the flux from the cathode spot is simplified to a sketch. Mattox has suggested that the energy dissipated at the cathode spot is approximately shared as follows: heat 34%, electron emission 21%, evaporation (atomic and macro) 3%, ionization (7%), energy to ions (23%), and energy to electrons (10%).⁸ Together with a very high ion density, the relatively high energy of ions in cathodic arc discharges make them very unique in thin film deposition processes. These

properties can be useful as well as detrimental to quality when growing thin films with cathodic arc discharges.

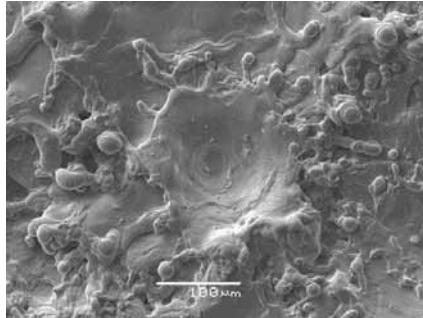


Figure 3.3: SEM image of a cathode spot and its vicinity (Al cathode, 14 A Filter Current, 20 V Burning Voltage, 110A Cathode Current after operation at 10^{-4} Pa)

The image of a cathode spot can be seen in Figure 3.3. The spot is surrounded by round morphological features. These are the remnants of the molten metal that is spread out of the cathode spot as the arc was burning there.

It is important to maintain anode conductivity during processing. If the anode is coated with a thick oxide film, the anode becomes isolated which may result on process instabilities.

3.2.2 The Ion Transfer

One of the strongest arguments against film growth with cathodic arc discharges has been the macroparticle issue. Macroparticles have been shown to be detrimental to thin film properties for some applications. One possibility to avoid macroparticle inclusion in to thin films is a magnetic filter. There are different designs of filters communicated in the literature, and their efficiencies are studied.^{9,10}

Electrons are extracted into the filter, and the positive ions follow the electron trajectories. The physics of this extraction are in fact very complicated and can be found on pages 305-325 of Anders' book.⁴ Once extracted, the electrons keep following the magnetic field lines through the filter. As they are followed by the ions, the ions are transported through the filter too. With the help of a magnetic field scanning unit the film forming species leaving the filter is uniformly distributed over the substrate surface. The magnetic field application in the filter increases the travelling path and therefore the time the electrons need to pass the plasma. It was reported earlier that this may enable an increased ionization of the residual gas species as well as the intentionally introduced species.¹¹ The influence of the magnetic field on the plasma composition in this work will be discussed later in chapter 5.

3.2.3 The Sheath

When the plasma beam finally reaches the substrate region, the kinetic energy of the species can be simplified described by the following equation: $E_T = E_i + E_k$, where E_T is the total energy of the ion as it approaches the substrate surface, E_i is the energy of the ion before entering the sheath and E_k is the kinetic energy gain of an ion as it is accelerated through the sheath. The kinetic energy is given by $E_k = (Q \cdot e \cdot \Delta U)$, where Q is the charge state of the ion, e is the elementary charge, and ΔU is the potential difference between the plasma and the substrate. The energy of the impinging ion can therefore be controlled by the use of a substrate bias potential.

-
- ¹ Priestley J. The History and Present State of Electricity with Original Experiments, 3rd Ed. Vol. 2, 260-276, London (1775)
- ² Anders A. IEEE Trans. Plasma Sci. **31** 1052-1059 (2003)
- ³ Anders A. IEEE Trans. Plasma Sci. **31** 1060-1069 (2003)
- ⁴ Anders A. Cathodic Arcs: From Fractal Spots to Energetic Condensation Springer, New York (2008)
- ⁵ Stafford K. N. et al. Surface Engineering Processes and Applications, Crc Pr Inc (1994)
- ⁶ Boxman R. L. et al. Handbook of Vacuum Arc Science and Technology, Noyes Publ. (1996)
- ⁷ Anders A. et al. IEEE Trans. Plasm. Sci. **20**, 466-472 (1992)
- ⁸ Mattox D. M. Handbook of Physical Vapor Deposition (Pvd) Processing, Noyes Publ. (1998)
- ⁹ Anders S. et al. IEEE Trans. Plasm. Sci. **21**, No.5 440-446 (1993)
- ¹⁰ Shi, X. et al. Int. J. Mod. Phys. B **14**, 136-153 (2000)
- ¹¹ J.M. Schneider et al. Appl. Phys. Lett. **78**, 150-152 (2001)

4. Characterization Techniques

In this chapter, the characterization techniques used in this study will be explained. Here were two main items to characterize: The plasma and the thin films deposited from this plasma. The plasma was characterized by a mass spectrometer coupled with an energy filter and a Langmuir probe. The thin film analyses were made by wavelength dispersive x-ray analysis (WDX), x-ray diffraction (XRD), electron microscopy, and nanoindentation.

4.1 Plasma Characterization

4.1.1 Mass Spectrometry

A mass energy analyzer (MEA) was employed to characterize the plasma. This device is in principle a mass spectrometer with an energy filter that is attached to the front. (Figure 4.1) The ions are extracted from the plasma through an orifice (Zone 1 in Figure 4.1). Zone 2 is an ion transfer optic system, which is also used as an ion formation room during neutral species measurements. The ions then enter the energy filter, zone 3. The ions leaving the energy filter pass through the mass filter in zone 4 before they reach their final destination, the secondary electron multiplier, where they are counted.¹

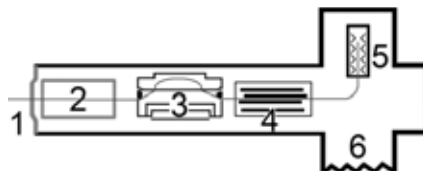


Figure 4.1: Mass Energy Analyzer (1 = Orifice, 2 = Ion Transfer, 3 = Energy Filter, 4 = Quadrupole Mass Filter, 5 = Secondary Electron Multiplier, 6 = Pumps)

4.1.1.1 Extraction Orifice (Zone 1 in Figure 4.1)

The pressure within the MEA needs to be a few orders of magnitude lower than the working pressure of the cathodic arc discharge. In order to keep a pressure difference between the deposition chamber and the MEA, an orifice of 100 μm is employed. The MEA system is sealed completely, except this 100 μm hole in the orifice, and a separate fore-vacuum and turbomolecular pump system maintains the pressure within the MEA at pressures below 10^{-5} Pa, while the pressure within the deposition chamber is as high as 2-3 Pa.

4.1.1.2 Optical Ion Transfer System (Zone 2 in Figure 4.1)

The system is primarily employed for ionizing the neutrals when the neutrals in the deposition chamber are measured. These may be residual gas molecules or depositing neutrals such as metallic species. During the measurement of ionic species, the electric fields within the system focus the ions extracted from the plasma and direct them towards the energy filter. This also has the additional advantage that the sensitive components face much less contamination by the species extracted from the plasma.

4.1.1.3 Energy Filter (Zone 3 in Figure 4.1)

The cylindrical mirror energy analyser (CMA) or in short energy filter consists of two cylinders built together, where one has a smaller radius than the other. These cylinders have very small entry and exit points as can be seen in Figure 4.1, and an ion beam of an exact energy step can be filtered by adjustment of the potentials U_{mirror} and U_{center} which correspond to the potentials of the outer and inner cylinders, respectively.

4.1.1.4 Mass Filter (Zone 4 in Figure 4.1)

The quadrupole mass filter consists of four 8 mm molybdenum rods where opposing rods are electrically coupled together. A RF potential is applied between the pairs of rods. An optimized direct current applied together with the RF potential enables only those ions with a certain mass to charge ratio to travel between the rods. The rest of the ions will be deflected and will not be able to traverse the path through the rods. By changing the voltages, a mass/charge analysis of up to 512 amu allows for composition analysis.

4.1.1.5 Secondary Electron Multiplier (Zone 5 in Figure 4.1)

An electron multiplier is a fast ion current amplifier. The ions leaving the mass filter are deflected 90° and are led to the first stage of the secondary electron multiplier. An ion hitting the first stage of the multiplier releases an electron, which then hits the second stage where more electrons are released etc. The 90° off axis orientation also assures that neutral species are filtered out, resulting in a lower noise level.



Figure 4.2: Langmuir Probe

4.1.2 Langmuir Probe

The Langmuir probe, named after the 1932 Nobel Prize winner, Irving Langmuir, is a tool used to determine the electron temperature, electron density, and the potential in a plasma.² In principle it is a rod put into the plasma to measure the

potential. The variable potential on the rod is adjusted while measuring the current that flows from the plasma. (Figure 4.2) An I-V graph is plotted from the data, and the above mentioned plasma properties can be extracted from this graph. The measurement rod is kept at small dimensions (10mm length <1mm radius) in order to minimize the influence on the plasma.

4.2 Film Characterization

4.2.1 Chemical Composition Analysis

The chemical composition of the samples was characterized using Wavelength Dispersive X-Ray Analysis (WDX), which uses x-rays to identify and quantify the elements in a sample. (Figure 4.3) In order to do so, WDX separates the x-ray into individual wavelengths which are detected at different spectrometer positions. The photons emitted from the sample are then collected and counted.³ The chemical composition of the deposited film was analysed using the Al K_{α} , O K_{α} , Ti K_{α} , and N K_{α} fluorescence lines and Al_2O_3 , Ti, and Fe_4N standards.

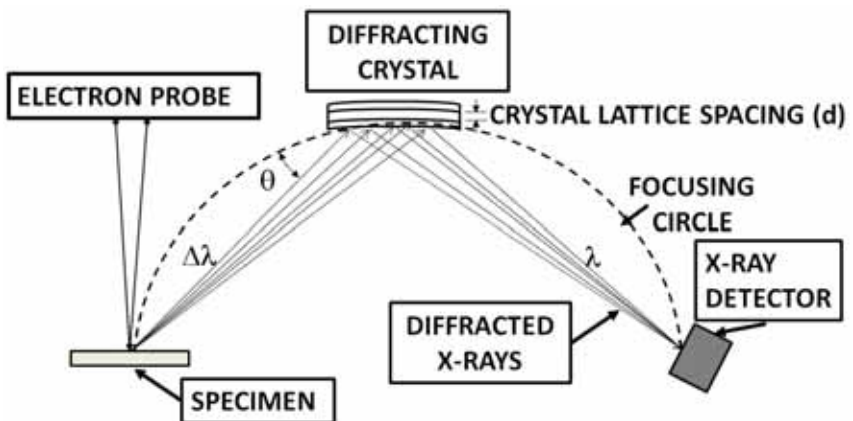


Figure 4.3: The principle of wavelength dispersive x-ray diffraction⁴

4.2.2 Structural Analysis

X-Ray diffraction was used to identify the crystal structure and the average grain size of the thin films. For crystal structure determination, the grazing incidence x-ray diffraction method was used where the x-ray incidence angle is kept at angles below 5°.

According to the Bragg's law, $2d\sin\theta=n\lambda$, the plane spacings, d , can be calculated, provided that λ and θ are known. λ , the wavelength of the X-Rays is determined by the anode material and the filters in the x-ray equipment. θ is the value of the diffraction angle. This way it is possible to determine the lattice distance values at a series of crystalline planes which are unique for every crystal. Thus, the structure of a crystalline material can be identified using x-ray diffraction.⁵

The grain sizes were determined from XRD data obtained by using the Bragg Brentano geometry. When the grain size is small (<100nm), a broadening of the diffraction peaks is observed. The extent of this broadening is given by the equation: $B = \frac{0.9\lambda}{t \cos \theta}$, where B is the broadening of diffraction line measured at half its maximum intensity (radians) and t is the grain size.⁵ The grain size value can be further refined by a series of alternative methods, but it is shown in this study that the formula above gives grain size values that are very close to the values provided by electron microscopy.

4.2.3 Morphology and Microstructure

In order to study the morphology and microstructure of the films, field emission scanning electron microscopy (FESEM, ZEISS DSM 982 Gemini) and transmission electron microscopy (TEM, FEI Tecnai F20 & JEOL JEM 2000 EX II) were employed.

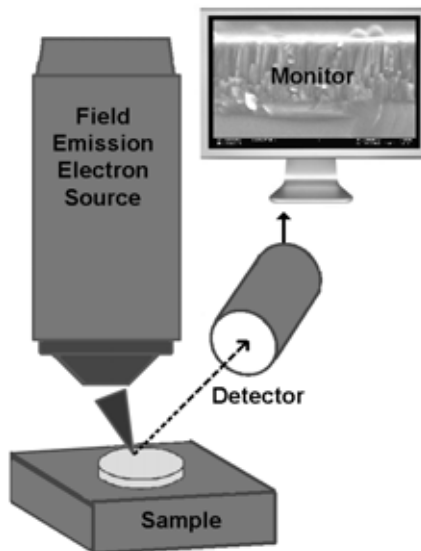


Figure 4.4: Field Emission Scanning Electron Microscope (FESEM)

The SEM working principle is shown in Figure 4.4. A highly focused electron beam is impinged on the sample which is to be measured. These electrons carry significant amounts of energy and upon impinging on the sample surface this energy is dissipated, resulting in a variety of signals. These signals include secondary electrons, backscattered electrons, diffracted backscattered electrons and x-rays. The secondary electrons are used to create the SEM images, the backscattered electrons carry information on the composition and crystal orientation, the diffracted

electrons are used for determining the crystal structure and texture, while x-rays are used to identify the chemical composition of the sample. FESEM has advantages compared to the more common SEM with a thermal emitter, most important being the higher resolution and reduced charging of the sample at lower acceleration voltages.⁶

For an even closer look at the morphology and microstructure, transmission electron microscopy (TEM) can be employed. Unlike SEM, TEM is based on thin specimens requiring a relatively difficult and time consuming sample preparation, thus only samples of special interest were studied by TEM.

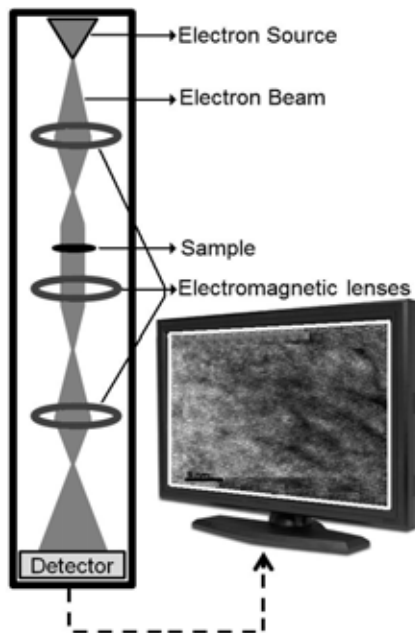


Figure 4.5: Transmission Electron Microscope (TEM)

As the name implies, in transmission electron microscopy the electrons are transmitted through the sample to be measured and are then recorded behind it on a

film or on a digital detector (CCD Camera). (Figure 4.5) The samples are very thin, in the order of 100 nm, thus electrons with very high energies can traverse them. TEM image resolution is significantly higher than that of SEM owing to the very small de Broglie wavelength of the electrons.⁷

The part of the electrons that is not transmitted through but were deflected by the sample atoms will be elastically scattered at particular angles which are determined by the crystal structure of the sample. Using this diffraction data, the local crystal structure can be determined. This method is often referred to as selected area electron diffraction (SAED).

4.2.4 Mechanical Property Analysis

A nanoindenter (Hysitron) has been used for mechanical property analysis. The nanoindenter is similar to a conventional indenter, but due to a very small tip size, and high resolution force and distance measurements on the nm scale can be extracted. This enables its use for elastic modulus and hardness measurements in thin films as thin as a few hundred nanometers. As soon as the tip has mechanical contact with the surface, the mechanical force is converted into an electrical signal by piezo crystals. (Figure 4.6)

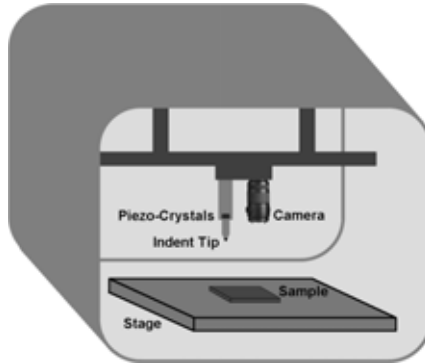


Figure 4.6: Nanoindenter

The tips used in this work are Berkovich type which is a four sided pyramid, where each side is exactly identical to the others. The tip radius is defined by the producer as 100nm. As it is used, the dimensions of the tip change. A tip area function is calculated with respect to a standard fused silica before each measurement set. This way, the exact shape of the tip is counted for. The load displacement data are used to calculate the elastic modulus and hardness values. Oliver and Pharr published a method, named after them, in 1992.⁸ The basic assumption here is that upon unloading deformation is purely elastic. This way the

following formula $\frac{1}{E_r} = \frac{(1-\nu^2)}{E} + \frac{(1-\nu_i^2)}{E_i}$ was presented, where E_r is the reduced elastic modulus of the sample, E is the elastic modulus of the sample, E_i is the elastic modulus of the indenter, ν is the Poisson's ratio of the sample, and ν_i is the Poisson's ratio of the indenter. The experimentally measured stiffness $S=dp/dh$ can be used to calculate the reduced elastic modulus E_r , using the following formula

$$S = \frac{dp}{dh} = \frac{2\sqrt{A}}{\sqrt{\pi}} E_r, \text{ where } A \text{ is the projected area of the elastic contact.}^8$$

The nanoindenter can also be used in AFM mode where the tip scans the surface at a constant load mode. This way the AFM images as well as surface roughness values can be extracted from the data measured by the nanoindenter.

¹ Operating Instructions, BG 805 813 BE (0306) PPM 422, Pfeiffer Vacuum

² I. Langmuir, Science 58 (1502): 290-291 (1923)

³ ASM Metals Handbook, Volume 10, Materials Characterization (1986) 180-181

⁴ Physical Methods for Materials Characterisation, PEJ Flewitt, RK Wild (IOP Publishing) p. 270

⁵ B. D. Cullity, Elements of X-Ray Diffraction, Addison-Wesley Publ. CO., 149-151, 1956

⁶ J. Goldstein Scanning Electron Microscopy and X-Ray Microanalysis Springer Netherlands; 3rd ed. (2002)

⁷ D. B. Williams, C. B. Carter, Transmission Electron Microscopy, Kluwer Academic Publ. (1996)

⁸ W. C. Oliver and G. M. Pharr, J. Mater. Res., Vol. 7, No. 6, 1564-1583, June 1992

5. Results and Discussion

A selected part of the results the author's research work is presented here. The sections are separated according to the key experiments carried out. This enables a better coherency within the scientific question that is answered at the cost of some repetition between the sections.

5.1 Pressure dependence of the Al ion energy distribution functions during filtered cathodic arc thin film growth in an Ar, O₂ ambient

Filtered cathodic arc (FCA) discharges are known to produce highly ionized metallic vapour with comparatively large ion energies^{1,2,3}. The high degree of ionization enables the control of the flux, and the energy of the depositing particles by magnetic and electric fields which enables the deposition of fully dense films with large adhesion. These advantages, together with a comparatively large deposition rate, make cathodic arc deposition an industrially relevant thin film process technology.

During low pressure plasma processing it is well known that the plasma chemistry and the energetics influence constitution,^{4,5,6,7} density,⁸ optical properties,^{9,10} mechanical properties,¹¹ and electrical properties¹². The average ion energies in cathodic arc discharges are in the range of 20 to 150 eV^{13,14}. Furthermore, it is well known that collisions between the primary non-thermalized metal ion population and gas reduce the ion energy. This was reported by Bilek et al. in a Ti cathodic arc discharge as the N₂ pressure was increased, and in a Ti and Al cathodic arc discharge in N₂ and O₂^{15,16}.

Surface diffusion controls the phase formation as well as the morphology evolution during low temperature thin film processing⁷. Surface diffusion may be enabled via ion bombardment controlled by applying a bias to the substrate, where the ions are accelerated towards the substrate and impinge with energies corresponding to $E=E_i+Q\cdot e\cdot(V_p-V)$, where E_i is the initial energy of the ion, Q the charge state, V_p the plasma potential, and V the substrate bias potential. Higher charge state ions may, consequently, possess energies up to several hundreds of eV. See for example Rosén et al.¹⁷ where the Al^{3+} ion with an average energy of 111 eV was reported. If a substrate bias potential of -200V is applied and a plasma potential around 1 eV exist, the average Al^{3+} ion energy is:

$$111\text{ eV}+3\cdot[1-(-200)]\text{eV}=714\text{ eV}.$$

It is well known that cathodic arc discharges contain a significant amount of multiple charged ions.^{18,19} It is challenging to study thin film structure evolution when several charge states co-exist. Rosén et al. reported that the presence of multiple charge states may be eliminated by increasing the deposition pressure resulting in an average ion charge state of 1.0 in Al cathodic arc discharge¹³. Both Rosén et al.¹³ and Bilek et al.¹⁶ reported agreement between their experimental ion energy distribution functions (IEDFs) and a superposition of two shifted Maxwellian distributions as proposed by Sherman²⁰ and later adopted by Kutzner and Miller²¹.

At an Ar pressure of approximately 1 Pa and cathode to substrate distance of 44 cm (pressure distance product of 44 Pa·cm)¹³, the IEDFs exhibits a high energy tail extending up to several hundreds of eV and a full width at half maximum of up to 67 eV. For studying the effect of ion energy on the structure evolution precise control over ion flux and energy are desired. Hence in addition to the presence of only single ionized metal ions, also a “narrow”, preferably monoenergetic IEDF is required. This has however never been reported in the literature.

Here, the effect of the gas pressure on the energetics and chemistry of an aluminium cathodic arc discharge is investigated. Our results indicate that a virtually monoenergetic Al^+ ion beam is formed at 256 Pa·cm due to collisions with the parent gas. This is a prerequisite for studying the effect of the ion energy on the phase formation without the effect of higher charge states and the presence of multiple populations in the IEDFs.

The potential difference between the Al cathode and the graphite anode was 21 V which agrees with the arc burning voltage of 22.6 V reported by Anders et al.¹⁴ The charge state resolved IEDFs of Al^+ , Al^{2+} , and Al^{3+} were measured with a mass energy analyzer (MEA, PPM 422, Pfeiffer Vacuum) in the pressure distance product range from 0.01 to 256 Pa·cm. The cathode to the grounded mass energy analyzer sampling orifice distance was 120 cm and the orifice diameter was 100 μm . Using a quadrupole mass spectrometer with an attached energy filter, the plasma chemistry can be determined through mass to charge measurements at constant energy and IEDFs are measured at constant mass to charge ratios.

The ion energy distribution functions (IEDFs) of Al^+ ions are plotted as a function of the pressure distance product (Figure 5.1.1). The IEDF at the lowest pressure distance product of 0.01 Pa·cm is rather broad with an energy tail extending up to 110 eV. As the pressure distance product is increased, metal ions may undergo collisions with the gas resulting in a lower average energy and a narrower ion energy distribution function. As metal ions scatter with gas atoms or molecules, their directed energy is reduced. This is henceforth referred to as thermalization.¹⁶ Bilek et al.^{15,16} and Rosén et al.¹³ report energy distribution function changes caused by neutral-ion collisions with the background gas resulting in the formation of IEDFs comprised of a thermalized metal ion population as well as a high energy population, similar to the

IEDFs presented here for $p \cdot d < 16 \text{ Pa} \cdot \text{cm}$. The distributions from ref. 13, 15, 16, 17 always included a high energy tail. As the pressure distance product is increased to $256 \text{ Pa} \cdot \text{cm}$, the distribution exhibits no measurable high energy tail. At room temperature and $5.7 \cdot 10^{-5} \text{ Pa}$, the mean free path of Al in Al is approximately 0.5 km , here Al ion collisions are unlikely, the mean free path increases to approximately 2.7 m at $1 \cdot 10^{-2} \text{ Pa}$ and to approximately 27 cm at 0.1 Pa , whereas at 2.13 Pa the mean free path of Al in Ar is approximately 1.3 cm and Al^+ ions will therefore collide with Ar on route to the mass energy analyzer. Hence, multiple collisions are to be expected for Al ions traversing the 120 cm source to substrate distance.

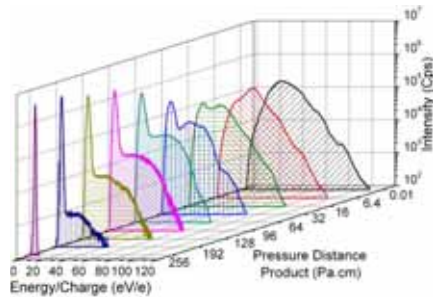


Figure 5.1.1: Al^+ ion energy distribution functions (IEDFs) as a function of pressure distance product

The average energy is calculated according to equation 5.1.1, where E_{avg} is the average energy (eV), Q the charge state, I the intensity at the energy step, and E the measured energy per charge ratio (eV/charge).

$$E_{\text{avg}} = \frac{\sum QIE}{\sum I} \quad (5.1.1)$$

In Figure 5.1.2(a), the average energy of Al ions is presented as a function of the pressure distance product. The average energies are decreased as the pressure distance product is increased. In Figure 5.1.2(b), the average charge state is plotted

as a function of the pressure distance product. The average charge state is decreased from 1.6 at 0.01 Pa·cm to 1.0 at pressure distance products larger than 32 Pa·cm. This is consistent with the data presented by Rosén et al.¹³ despite the different plasma sources employed. However, at lower pressure distance products, Rosén et al.¹³ report higher energies compared to the data presented here. This may be due to the influence of different gas flow and entry point in these two systems. Tarrant et al. showed that gas flow and entry point influences the IEDF of the species in an arc discharge.²² The size and number of arc spots burning on the cathode, arc current, burning voltage as well as the applied magnetic fields are other possible sources for the energy difference discussed above.

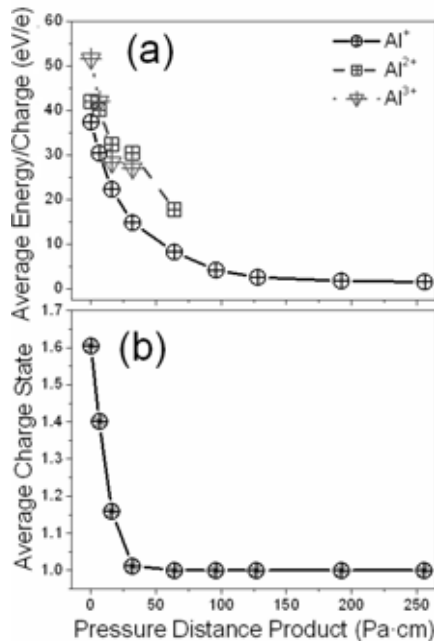


Figure 5.1.2: (a) Average energy of Al⁺, Al²⁺, and Al³⁺ ions and (b) average charge state of Al ions as a function of pressure distance product

The pressure dependence of IEDFs of Al^{2+} and Al^{3+} are presented in Figures 5.3(a) and (b). At base pressure the ratio of Al ions is as follows: 50% Al^{2+} , 46% Al^+ and 4% Al^{3+} . As the pressure is increased, the Al^{2+} ion population, which is the dominant species at 0.01 Pa·cm, is decreased and is annihilated at pressures above 64 Pa·cm. Similar changes are observed for the Al^{3+} ion population which can not be detected at pressures above 16 Pa·cm. Al^{2+} and Al^{3+} ions undergo charge exchange collisions resulting in decreased energy, charge state, and signal intensities. This is consistent with the results presented by Rosen et al.¹³

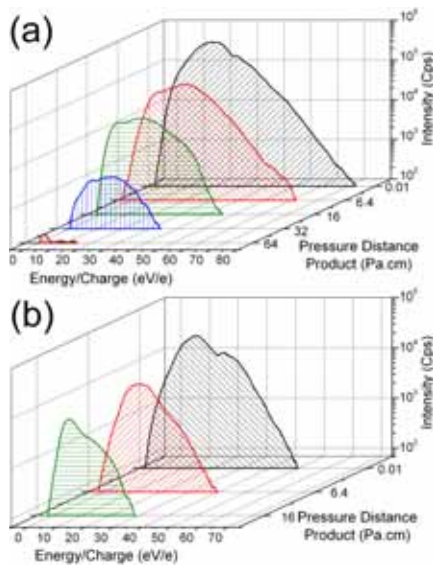


Figure 5.1.3: a) Al^{2+} and b) Al^{3+} ion energy distribution functions (IEDFs) as a function of the pressure distance product

In Figure 5.1.4, the Al^+ IEDFs in pure Ar and in a 50 at. % Ar - 50 at. % O_2 mixture at 128 Pa·cm is presented. Similar IEDF's are observed for an Ar/ O_2 mixture and for pure Ar indicating a comparable thermalization effect. The average energy of

the Al^+ IEDF in Ar is 2.6 eV with a FWHM of 2.1 eV. In Ar-O the average ion energy is 1.4 eV with a FWHM of 1.6 eV.

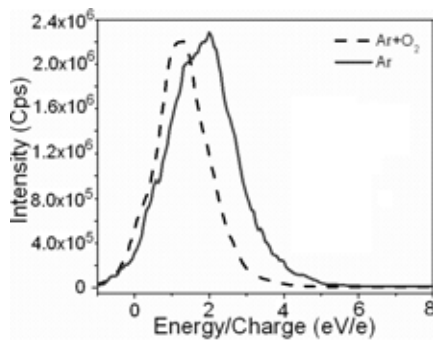


Figure 5.1.4: Al^+ ion energy distribution functions (IEDFs) at 128 Pa·cm in Ar and Ar+O₂ mixture

A thin film was grown on a TiAlN coated Si wafer at -200 V substrate bias and 700 °C substrate temperature. The stoichiometry of the film measured by WDX showed an O/Al ratio of about 1.5 which corresponds to stoichiometric Al_2O_3 . The structure of the film was analysed by grazing incidence (1°) XRD with a Cu tube (Figure 5.1.5). The TiAlN film has peaks at 2θ values of 37.5° , 43.6° , 63.2° and 75.5° which correspond to the reflections from the (111), (200), (220) and (311) planes of the cubic TiN structure according to JCPDS card nr. 38-1420. The major peaks of the deposited alumina film which do not overlap with the substrate peaks from TiAlN are observed at 2θ values of 45.5° and 66.7° , which correspond to the (400) and (440) planes of the $\gamma\text{-Al}_2\text{O}_3$ phase according to the JCPDS cards 10-425 and 29-63. The peaks at 37.5° and 39.5° correspond to reflections from the (311) and (222) planes of the $\gamma\text{-Al}_2\text{O}_3$ phase according to the same JCPDS cards. Two small peaks at 2θ positions 34.9° and 52.4° may stem from the (104) and (024) planes of the $\alpha\text{-Al}_2\text{O}_3$

phase according to the JCPDS card nr. 46-1212. The deposition rate was about 110 nm/min resulting in a film thickness of approximately 3µm.

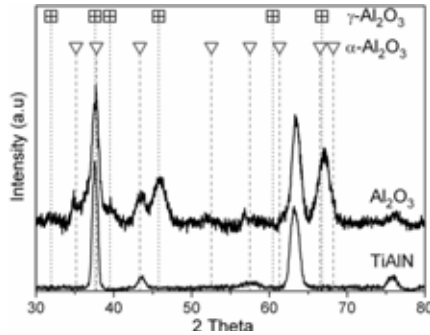


Figure 5.1.5: XRD pattern of a film grown in an Ar-O₂ gas mixture at 128 Pa·cm

The applicability of the here suggested synthesis strategy, namely to create a single charged monoenergetic ion beam is constrained by the associated flux loss. The flux of Al ions is calculated from the integrated IEDFs. The flux loss is defined in equation 5.1.2, where E stands for the measured energy/charge ratio, Q the charge of Al ions, and I the measured intensity in counts per second.

$$Fluxloss(\%) = \left[1 - \frac{\sum_{Q=1}^{Q=3} EI_Q^{InvP}}{\sum_{Q=1}^{Q=3} EI_Q^{baseP}} \right] \cdot 100 \quad (5.1.2)$$

As the pressure distance product is increased from 0.01 Pa·cm to 6.4 Pa·cm the flux decreases by 51%. At 256 Pa·cm, the flux is decreased by 75% with respect to the flux obtained at 0.01 Pa·cm. It can also be seen that within the region where aluminium oxide films are grown (64-192 Pa·cm) the flux loss is in the range of 58-64%. This flux loss is relatively small compared to the flux loss in the work of Rosén

et al. [13] which was reported to be >99.7% at 44 Pa·cm with respect to the flux at base pressure. This may be due to more efficient transfer through the filter.

The IEDFs of Al⁺ were fitted by the least square method using the distribution suggested by Kutzner and Miller [21] [Eq. (5.3)] and used by Bilek et al. [16] for the presence of non-thermalized and thermalized metal ion populations.

$$f(E) = C (E - QV_p) \exp \left[- \frac{\left((E - QV_p)^{1/2} - (E_{dir})^{1/2} \right)^2}{T} \right] \quad (5.3)$$

where C is a scaling constant, Q the charge state, V_p the plasma potential with respect to ground, E_{dir} the directional energy (centre of mass energy), and T the ion temperature (random energy).

Employing many fitting parameters enables multiple fit solutions. For the best fit (smallest error function), the plasma potential was measured in advance with a Langmuir probe and was found to decrease from 3 to 1 V as the pressure distance product was increased from 0.01 Pa·cm to 256 Pa·cm. The measured plasma potentials are used in the fitting process.

The IEDFs with their corresponding fits are presented in Figure 5.1.6 with linear intensity scales. Figure 5.1.6(a) shows the Al⁺ IEDF at 256 Pa·cm where the plasma consists of a single thermalized metal ion population and thus the IEDF can be fitted with equation 5.1.3. Figure 5.1.6(b) shows the fit of the Al⁺ IEDF at 16 Pa·cm. The experimental IEDF can be fitted only with a superposition of equation 5.1.3 applied to the non-thermalized and thermalized metal ion populations. The first part of the fit at lower energies represents the ions which belong to the thermalized metal ion population, whereas the second part of the fit represents the non thermalized metal ion population. Figure 5.1.6(c) shows the fit of the Al⁺ IEDF at 0.01

Pa·cm. The experimental IEDF can be fitted with equation 5.1.3 where the plasma consists of a single non-thermalized metal ion population.

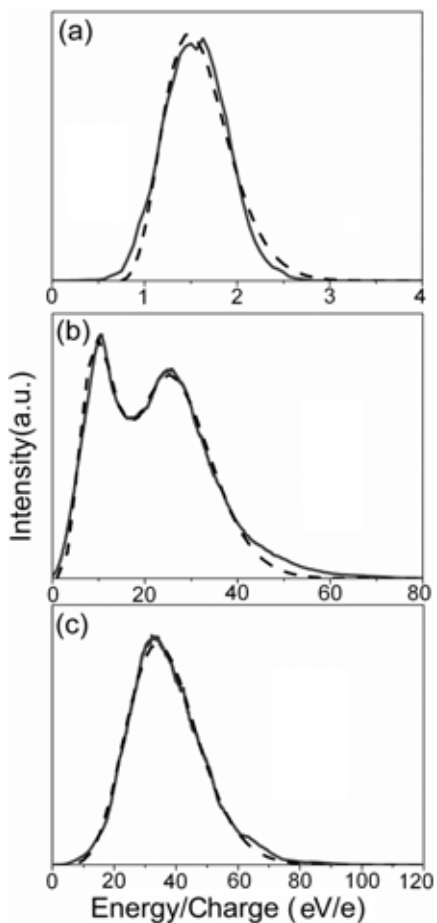


Figure 5.1.6: Al⁺ ion energy distribution functions (IEDFs) and the fitting curves (a) at 256 Pa·cm (b) at 16 Pa·cm, and (c) at 0.01 Pa·cm

In Figure 5.1.7, the directional (E_{dir}) and random energies (T) of the thermalized ($E_{dir,t}$, T_t) and non-thermalized ($E_{dir,nt}$, T_{nt}) metal ion populations are

plotted as a function of the pressure distance product. The thermalized ion population partially preserves its directionality at low pressure distance products. The directional energies of both ion populations ($E_{dir,t}$, $E_{dir,nt}$) decrease as the pressure distance product is increased (see Figure 5.1.7a). This is consistent with the notion of the energy loss of Al^+ ions in collisions with Ar. The random energy of the thermalized metal ion population (T_t) decreases slightly with an increasing pressure distance product due to the higher number of collisions (see Figure 5.1.7b). On the other hand the random energy of the non-thermalized metal ion population (T_{nt}) increases with an increasing pressure distance product. This may be due to the energy dependence of the scattering cross section, resulting in a more efficient thermalization of ions with lower energy compared to the high energy fraction of the population. The error bars are included in Figure 5.1.7 and they are generally insignificant. However, the intensity of the non-thermalized ion population at pressure distance products above 128 Pa·cm is very small resulting in larger errors in both $E_{dir,nt}$ and $T_{dir,nt}$.

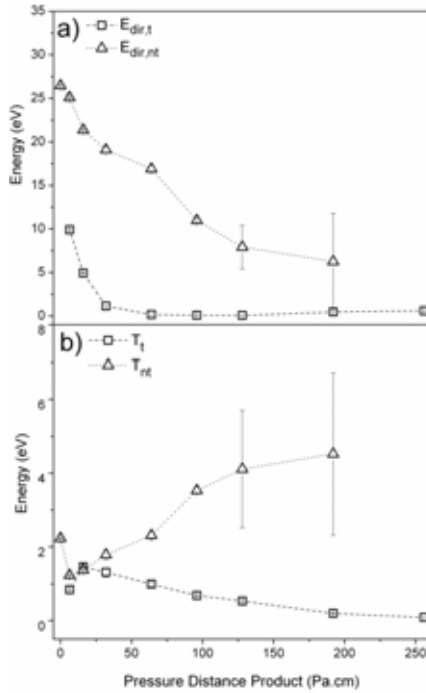


Figure 5.1.7: Directional (a) and random (b) energies $E_{dir,t}$, $E_{dir,nt}$, T_t and T_{nt} for Al^+ fits as a function of pressure distance product

-
- [1] Randwaha H and Johnson P C 1987 Surf. Coat. Technol. **31** 4-303
- [2] Boxman R L Martin P J and Sanders D M 1996 *Handbook of Vacuum Arc Science and Technology* (Norwich: William Andrew Publishing)
- [3] Anders A 2000 *Handbook of Plasma Immersion Ion Implantation and Deposition* (Weinheim: Wiley-VCH)
- [4] Schneider J M Larsson K Lu J Olsson E and Hjörvarsson B 2002 Appl. Phys. Lett., **80**, No. 7, 1144
- [5] Mráz S and Schneider J M 2006 Plasma Chem. Plasma Process. **26**,197
- [6] Rosén J Mráz S Kreissig U Music D and Schneider J M 2005 Plasma Chem. Plasma Process. **25**, 4, 303
- [7] Petrov I Barna P B Hultman L and Greene J E 2003 J. Vac. Sci. Technol. A **21/5**, S117
- [8] Thornton J A 1974 J. Vac. Sci. Technol. **11/4**, 666
- [9] Anders S Anders A Rubin M Wang Z Raoux S Kong F and Brown I G 2002 Surf. Coat. Technol. **76-77**, 167
- [10] Tay B K Zhao Z W and Sun C Q 2005 Surf. Coat. Technol. **198**, 94
- [11] Bendavid A Martin P J Wang X Wittling M and Kinder T J 1995 J. Vac. Sci. Technol. A **13/3**, 1658
- [12] Chua D H C Teo K B K Tsai T H Robertson J and Milne W I 2002 J. Modern Phys. B, **16/6-7**, 830,
- [13] Rosén J Anders A Mráz S Atiser A and Schneider J M 2006 J. Appl. Phys. **99**, 12303
- [14] Anders A and Yushkov G Y 2002 J. Appl. Phys. **91**, 4824
- [15] Bilek M M M Chowalla M and Milne W I 1997 Appl. Phys. Lett. **71**, 13, 1777
- [16] Bilek M M M Martin P J and McKenzie D R 1998 J. Appl. Phys. **83**, 6, 2965
- [17] Rosén J Anders A Mráz S and Schneider J M 2006 J. Appl. Phys. **97**, 103306
- [18] Rosén J Anders A and Schneider J M 2002 Appl. Phys. Lett. **80**, 22, 4109
- [19] Rosén J Anders A and Schneider J M 2006 Appl. Phys. Lett. **89**, 141502
- [20] Sherman J C 1972 University of Liverpool Report ULAP-10 (unpublished)
- [21] Kutzner J and Miller H C 1992 J. Phys. D: Appl. Phys. **25**, 686,
- [22] Tarrant R N Bilek M M M Oates T W H Pigott J and McKenzie D R 2002 Surf. Coat. Technol. **156**, 110

5.2 Influence of plasma chemistry and ion flux on the phase formation and the deposition rate of Al₂O₃ films grown with cathodic arc

Crystalline Al₂O₃ thin films are of interest to a broad part of the industrial and scientific community due to their applicability in fields ranging from corrosion,¹ catalytic support,² diffusion barrier,³ and wear protection⁴ to microelectronics.⁵

α-Al₂O₃ is the thermodynamically stable phase. γ-Al₂O₃ was shown to be thermodynamically stable at specific surface areas higher than 125 m²/g due to its lower surface energy.⁶ Besides α-Al₂O₃ and γ-Al₂O₃ phases, numerous metastable alumina phases such as, δ, η, θ, κ, β, and χ-Al₂O₃ exist.⁷ It is reported that⁸ the γ-Al₂O₃ phase can be stable at temperatures up to 1170°C. This may enable the γ-Al₂O₃ phase to be employed on cutting tools, machining, and chipping applications.

Alumina thin films can be synthesized by various deposition techniques. Chemical vapor deposition (CVD),⁹ where the substrate temperature is well above 1000°C, is the most established method. Kyrylov et al.¹⁰ produced γ-Al₂O₃ thin films with plasma enhanced chemical vapor deposition (PECVD), where they used the additional energy delivered to the surface by the ion bombardment to decrease the deposition temperature down to 500 °C. Magnetron sputtering has been used by Schneider et al.¹¹ to deposit thin films including κ-Al₂O₃ at temperatures as low as 320°C. Atiser et al. reported the formation of a phase mixture of γ-Al₂O₃ and α-Al₂O₃ in thin films coated using a filtered cathodic arc discharge.¹²

A high deposition rate of alumina thin films (up to 3.25 nm/s) by off plane double bend filtered cathodic arc technique has been reported by Choong et al.¹³ Besides high deposition rate, filtered cathodic arc (FCA) discharge is known to

produce highly ionized metallic vapor with high ion energies.¹⁴ The high ionization may enable a better control of the flux and energy of the depositing particles by magnetic and electric fields. Furthermore, the control of the plasma chemistry and energetics is important as they are known to influence the film properties.^{15,16,17}

There are only few publications on plasma chemistry and energetics of Al cathodic arc discharges. The ion energy distribution functions (IEDFs) were presented for Ti and Al cathodic arc discharges in reactive atmospheres, N₂ and O₂.¹⁸ Rosén et al. demonstrated the influence of Ar and O₂ on ion energy distributions of filtered aluminum arcs.¹⁹

The magnetic field often employed for plasma steering was shown to influence the plasma chemistry and energetics.^{20,21} Rosen et al. reported that introducing a magnetic field in an Al cathodic arc plasma resulted in higher average energies.²² Cathodic arc discharges were shown to contain significant amount of multiply charged ions,^{23,24} and these multiply charged species have higher energies in the presence of a magnetic field.²² However, none of these works comprised the influence of a gradual change in filter current on plasma chemistry and energetics of a cathodic arc discharge.

Here the influence of the filter current on plasma chemistry and energetics are presented. This knowledge is used to identify the effect of plasma chemistry and energetics on the phase formation, deposition rate, and growth morphology of alumina thin films grown with cathodic arc.

Alumina thin films were deposited on TiAlN coated Si wafers with a variation of the filter current from 10 to 20 A. The cathode to substrate distance was 120 cm,

while the gas inlet to cathode distance was approximately 136 cm. Aluminum cathodes with a diameter of 70 mm and a purity of 99.5% were used. The anode material was graphite. A scanner is installed at the end of the double bend offline filter which enables homogenous distribution of the plasma into the chamber (Fig. 3.1). The plasma scanning parameters (6x6 Matrix, 10 μ s interval), arc current (110 A-DC), anode coil current (9 A), the process pressure (1.0 Pa), substrate temperature (700°C), and bias (-200V) were kept constant for all experiments reported here. There was no surface treatment or preliminary etching of the substrates prior to deposition. The samples were heated to the peak temperature at approximately 10 K/min heating rates and were allowed to cool in vacuum at rates below 10 K/min.

Plasma chemistry and energetics were investigated by a mass-energy analyzer (MEA, Pfeiffer Vacuum, PPM-422) located at the same position as the substrate holder. An orifice with the size of 100 μ m was employed for the experiments. Using a quadruple mass spectrometer with an attached energy filter, this equipment can determine the plasma chemistry through mass to charge measurements at constant energy as well as extract IEDFs at constant mass to charge ratios.

The chemical composition of the deposited film was analysed by wavelength dispersive x-ray spectroscopy (Camebax SX 50) at 7 keV and 80 nA using the Al K α , O K α , Ti K α , and N K α fluorescence lines and Al₂O₃, Ti, and Fe₄N standards. The phases formed were identified by x-ray diffraction with 1° grazing incidence. (40 kV, 40 mA) The grain size was determined using the Debye Scherrer method from x-ray diffraction scans (Bragg Brentano, 40kV, 40 mA) with respect to LaB₆ standard.

The plasma chemistry and energetics data are presented in Fig. 5.2.1 The fractions of the dominant positive ions are shown in Fig. 5.2.1 (a) as a function of the filter current. Al^+ is the dominant ion up to filter current of 15 A. As the filter current is increased from 10 to 20 A, the population of the Al^+ ions decreases from 99.3% to 36.6%. The major population decrease for Al^+ occurs between 15 and 17 A, from 94.3% to 48.2%. Ar^+ and O^+/O_2^+ increase up to 54% and 9%, respectively, at 20 A. The other species which are considered to be relevant for thin film growth, such as H^+ , H_2^+ , were not individually measured as these ions were not detected in mass scans at peak energy values of gaseous species such as Ar^+ , O^+ and, O_2^+ .

The average charge state of Al ions is 1.0 for all filter currents. One possible explanation for the change in the plasma composition is the influence of the magnetic isolation of the anode,²⁵ which in turn increases the burning voltage from 21 V to approximately 28 V. In this case, it is conceivable that more magnetic field lines couple with the magnetic field of the filter, instead of the anode, and more electrons are directly extracted into the filter. This may contribute towards an increase of the electron density in the filter.

As the filter current is increased, the magnetic field strength is increased according to $B=C*I$ ($C=\mu_0*N/h$), where C is a constant including the permeability, length, and number of coils of the wire through which the filter current I passes. This increase is expected to be linear according to the formula above. At higher magnetic field strengths, it was explained earlier that the electrons would be trapped longer, resulting in an increased probability of electron impact ionization of the species within the filter.^{15,21} This may explain the increase in Ar and O populations as the filter current is increased.

The IEDFs of Al^+ ions are presented as a function of the filter current in Fig. 5.2.1(b). The most probable energy as well as the maximum energy of the Al^+ IEDFs does not change significantly as the filter current is increased from 10 to 20 A. Atiser et al.¹² reported earlier in a work based on the same deposition system and similar conditions that the IEDFs were thermalized as the pressure distance product is increased. This work was carried out at a pressure distance product of 128 Pa.cm, where the IEDFs were thermalized due to scattering. The peak intensity decreases by approximately two orders of magnitude as the filter current is increased from 10 to 20 A, while the integrated intensities decrease by an order of magnitude. The average energy of Al^+ ions decreases from 1.4 eV to 0.3 eV as the filter current is increased from 10 to 20 A. [Fig. 5.2.1(c)] The total ion flux also decreases one order of magnitude as the filter current is increased from 10 to 20 A, which is mainly due to the decrease of the Al^+ flux.

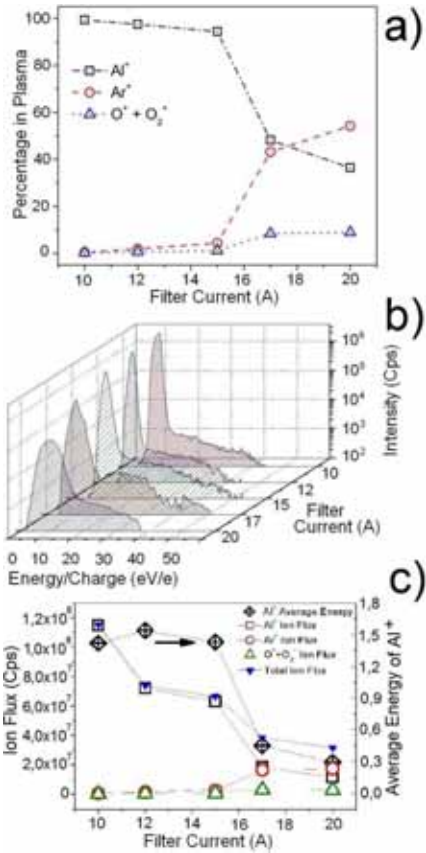


Figure 5.2.1: Plasma chemistry and energetics as a function of filter current: (a) the relative amounts of Al^+ , Ar^+ and O^+/O_2^+ , (b) Al^+ ion energy distribution functions (IEDFs), (c) ion fluxes of ions and total ion flux and average energy of Al^+ ions

The composition of the thin films was not influenced by the changes in plasma chemistry, and the O/Al ratio remained constant at $1.5 \pm 1\text{at}\%O$, which corresponds to the O/Al ratio of stoichiometric Al_2O_3 . (Figure 5.2.2) The sample at 10 A was too thin to be analysed quantitatively by WDX for composition.

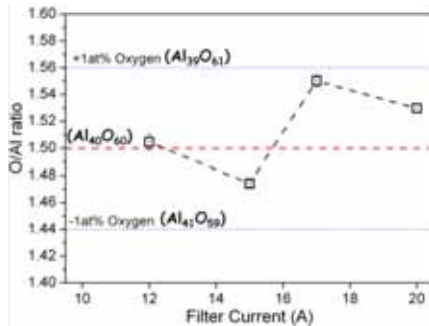


Figure 5.2.2: O/Al ratios as a function of the filter current

The structure of the films is presented in Fig. 5.2.3. The diffractogram of a TiAlN coated Si wafer is included for reference. There are four diffraction peaks visible for the TiAlN thin film at 2θ values of 37.3, 43.0, 62.9, and 75.4 degrees. These values are corresponding to the reflections from 111, 200, 220, and 311 planes for cubic TiN structure with approximately 1 degree shift due to Al presence in the lattice. The thin films grown at 10 and 12 A are XRD-amorphous, while the films grown at 15, 17, and 20 A are crystalline. There is no evidence for the presence of an additional phase in the diffraction data of the films grown at 17 and 20 A filter current, thus the films are pure γ - Al_2O_3 with the major peaks at 45.7° (400) and 66.7° (440) which represent the largest intensities according to JCPDS card: 10-425. The diffraction data for the film grown at 15 A shows a phase mixture of α - Al_2O_3 and γ - Al_2O_3 . We observe the 45.7° and 66.7° peaks for γ - Al_2O_3 together with 2 small peaks at 35.1° and 57.5° which correspond to the largest intensities of α - Al_2O_3 according to JCPDS card: 46-1212. Selected area electron diffraction measurements were carried out for all samples. These measurements confirmed the formation of γ - Al_2O_3 phase for the films grown at 15, 17, and 20 A. The samples grown at 10 and 12 A were found to be nanocrystalline. The film grown at 12 A was found to be a phase mixture

of α -Al₂O₃ and γ -Al₂O₃, while the film grown at 10 A was pure γ -Al₂O₃ according to SAED data. The samples 12 A and 15 A show the presence of the α -Al₂O₃ phase. As it was discussed earlier, the ion flux decreases significantly between 15 and 17 A. This may explain the formation of α -Al₂O₃ in samples grown at 12 and 15 A filter currents. The additional energy submitted to the surface via higher ion flux may activate surface diffusion and thus enable α -Al₂O₃ formation. The sample 10 A was too thin for XRD analysis (~200nm) as it will be discussed later in morphology section. It was reported earlier that the α -Al₂O₃ phase formed only after a γ -Al₂O₃ thin film is formed on the substrate where the γ -Al₂O₃ film thickness was 150-300 nm.²⁶ This may explain why only γ -Al₂O₃ is observed for the film grown at 10 A filter current despite the higher ion flux.

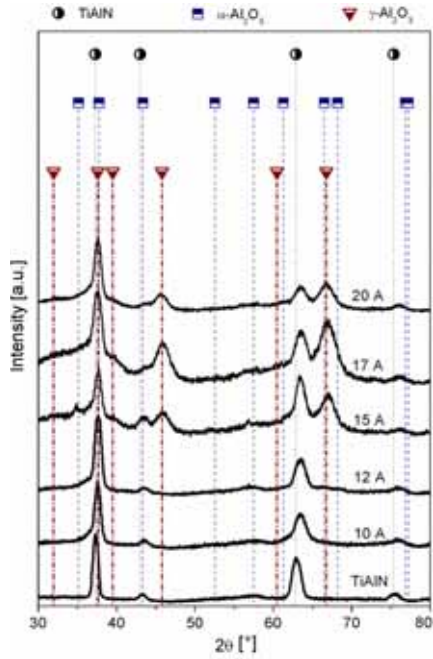


Figure 5.2.3: GIXRD data of thin films grown on TiAlN substrates for 10 to 20 A

The grain size was calculated based on Bragg Brentano geometry XRD measurements for the crystalline films with the Debye-Scherrer method.²⁷ The broadening due to equipment was measured with a LaB₆ standard and the respective correction was included in the calculations. The grain sizes were 23.5 nm, 21.1 nm, and 30.7 nm for samples grown at 15, 17, and 20 A filter currents.

It was shown earlier in Figure 5.2.1c that the ion flux decreases an order of magnitude as the filter current is increased from 10 to 20 A. Despite the decrease of ion flux, the deposition rate increases from 0.1 nm/s to 2.1 nm/s as the filter current is increased from 10 to 20A. This suggests that there are other physical mechanisms

that are active other than adsorption. As the ion flux and energies are relatively high, one possible mechanism is etching.

The deposition rate and etched flux are plotted as a function of the filter current in Figure 5.2.4. The etched flux of Al was calculated based on the Al sputtering yields, $Y_{Ar^+}^{Al}$ and $Y_{Al^+}^{Al}$, due to Ar^+ and Al^+ ion bombardment and the corresponding Ar^+ and Al^+ ion currents, I_{Ar^+} and I_{Al^+} , assumed to be proportional to the integrated Ar^+ and Al^+ energy distribution functions:

$$etched \ flux = Y_{Ar^+}^{Al} I_{Ar^+} + Y_{Al^+}^{Al} I_{Al^+}$$

The Al sputtering yields were calculated based on TRIM (transport of ion in matter) code with surface binding energies of 8.60 and 4.84 eV for Al and O, respectively. The surface binding energies were calculated based on a matrix model proposed for compounds for TRIDYN (dynamic transport of ions in matter) code with heat of Al atomization of 3.36 eV, heat of Al_2O_3 formation of 17.32 eV, and heat of O_2 dissociation of 5.12 eV.

The low deposition rate (at 10 A, 0.1 nm/s) corresponds to the highest etching (7.5×10^6), whereas the highest deposition rate (at 20 A, 2.1 nm/s) corresponds to the lowest etching (9.4×10^5). The data presented in Figure 5.2.4 present a possible explanation for the deposition rate increase with increasing filter current.

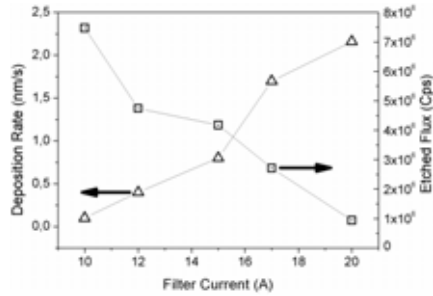


Figure 5.2.4: Deposition rate and etched flux as a function of the filter current.

Elastic properties and topography were measured by a nanoindenter (Hysitron) with a Berkovich type diamond indenter with a tip radius of 100nm. (Figure 5.2.5) Reduced elastic modulus values extracted from load-displacement curves were used for the calculation of the Young's modulus values according to the formula presented by Oliver and Pharr.²⁸ Elastic properties of α -Al₂O₃ are well known.²⁹ An α -Al₂O₃ standard was measured and the Young's modulus was found to be 6.8% higher than the literature value.

Schütze et al.³⁰ reported the elastic modulus of γ -Al₂O₃ to be 350 GPa. Gutiérrez et al.³¹ used *ab initio* calculations with local density approximation (LDA) to calculate the bulk modulus value for γ -Al₂O₃ structure of 219 GPa, which corresponds to a Young's modulus value of approximately 350 GPa, assuming a Poisson's ratio of 0,231 and hence elastic isotropy.

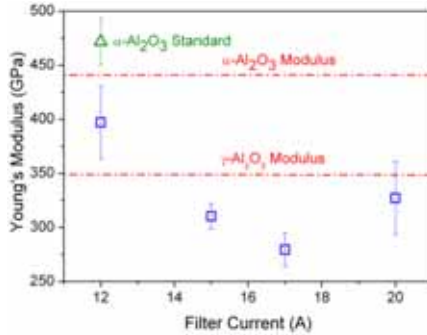


Figure 5.2.5: Young's modulus as a function of filter current

The average Young's modulus values for the γ - Al_2O_3 films grown at 15, 17 and 20 A are 310, 279, and 327 GPa, respectively. The Young's modulus at 20 A sample is 6.6% below the theoretical literature value.^{30,31} We may therefore conclude that the films are dense which is also supported by the SEM images. The Young's modulus value of the film grown at 12 A of 390 GPa is higher as compared to reported values of amorphous Al_2O_3 (<140 GPa)³² as well as for γ - Al_2O_3 . The nanocrystalline constitution of this film including α - and γ - Al_2O_3 was shown by selected area electron diffraction investigations. The Young's modulus values are primarily determined by the phase formed.

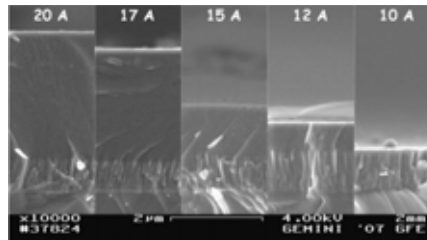


Figure 5.2.6: SEM cross-section images of all samples

The morphology of the films was studied with SEM and TEM. In Figure 5.2.6, the cross sections of all films are presented. The columnar TiAlN interlayer is visible

in all films with a thickness of 500-800 nm. As the Al_2O_3 deposition time was kept constant for all samples (1500s), the change in the deposition rate is straightforward. The film deposited at 20 A filter current has a deposition rate of 2.1 nm/s, while the film grown at 10 A has a deposition rate of only 0.1 nm/s. The SEM data do not provide evidence of any porosity or columnar growth.

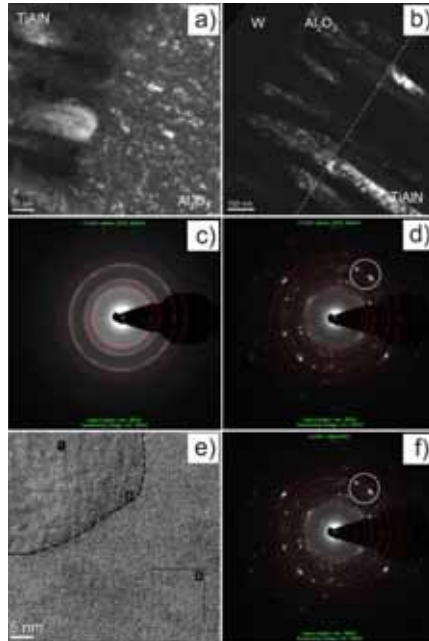


Figure 5.2.7: Darkfield images of samples a) 20 A and b) 12 A, for $\gamma\text{-Al}_2\text{O}_3$ simulations with superimposed reflection positions on selected area electron diffraction patterns of samples c) 20 A and d) 12 A, e) high resolution image from the TiAlN $\gamma\text{-Al}_2\text{O}_3$ interface, f) , $\alpha\text{-Al}_2\text{O}_3$ simulations with superimposed reflection positions on selected area electron diffraction patterns of sample 12 A

TEM and SAED data for the samples grown at 12 Å and 20 Å are presented in Figure 5.2.7. The darkfield image of a sample grown at 20 Å (Figure 5.2.7a) shows equiaxed grains grown on a columnar TiAlN film, while the columnar structure of the TiAlN film is transferred into the Al₂O₃ film for the sample grown at 12 Å (Figure 5.2.7b). This may be of interest as both morphologies may be useful for different applications. Local area electron diffraction patterns were obtained from both samples. A γ -Al₂O₃ simulation is consistent with the SAED data for the sample grown at 20 Å (Figure 5.2.1c), whereas both γ -Al₂O₃ and α -Al₂O₃ simulations are consistent with the SAED data for the sample grown at 12 Å (Figure 5.2.7d and 5.2.7f). This, together with the high Young's modulus (390 GPa) value measured in this film, suggests that a mixture of γ -Al₂O₃ and α -Al₂O₃ phases is present in this film. A high resolution image of the sample grown at 20 Å is shown in Figure 5.2.6e where the interface is crystalline.

-
- ¹ V.A.C. Haanappel, H.D. van Corbach, T. Fransen, P.J. Gellings, *Surf. & Coat. Technol.* 72, 13 (1995)
- ² C. R. Henry, *Surf. Sci. Rep.* 31, 231 (1998)
- ³ J. Mueller, D. Neuschuetz, *Vacuum* 71, 247 (2003)
- ⁴ D. Kurapov, J. Reiss, D. H. Trinh, L. Hultman, J. M. Schneider, *J. Vac. Sci. Technol. A* 25, 4, 831 (2007)
- ⁵ S. Y. Wu, M. Hong, A. R. Kortan, J. Kwo, J. P. Mannaerts, W. C. Lee, Y. L. Huang, *App. Phys. Lett.* 87, 091908 (2005)
- ⁶ J. M. McHale, A. Auroux, A. J. Perrotta, A. Navrotsky, *Science*, 277, 788 (1997)
- ⁷ G. Paglia, A. L. Rohl, C. E. Buckley, J. D. Gale, *Physical Review B* 71, 224115 (2005)
- ⁸ D. Kurapov, J.M. Schneider, *Steel Research Int.* 75, 9, 577 (2004).
- ⁹ A.R. Barron, *Insulating materials: W.S. Rees Jr. (Ed.), CVD of Nonmetals, VCH, Weinheim, 1996.*
- ¹⁰ O. Korylov, D. Kurapov, J. M. Schneider, *Applied Physics A* 80, 8, 1657 (2005)
- ¹¹ J. M. Schneider, W. D. Sproul, A. Matthews, *Surf. & Coat. Technol.* 98, 1/3, 1473 (1998)
- ¹² A. Atiser, S. Mráz, J. M. Schneider, *J. Phys. D: Appl. Phys.* 42 (2009) 015202
- ¹³ Y. S. Choong, B. K. Tay, S. P. Lau, X. Shi, Y. H. Cheng, *Thin Solid Films* 386, 1 (2001)
- ¹⁴ H. Randwaha, P. C. Johnson, *Surf. Coat. Technol.* 31, 4, 303 (1987)
- ¹⁵ J. M. Schneider, K. Larsson, J. Lu, E. Olsson, B. Hjörvarsson, *Appl. Phys. Lett.*, 80, 7, 1144 (2002)
- ¹⁶ S. Mráz, J. M. Schneider, *Plasma Chem Plasma Process* 26, 197 (2006)
- ¹⁷ J. Rosén, S. Mráz, U. Kreissig, D. Music, J. M. Schneider, *Plasma Chem Plasma Process* 25, 4 (2005)
- ¹⁸ M. M. M. Bilek, P. J. Martin, D. R. McKenzie, *J. Appl. Phys.* 83, 6, 2965 (1998)
- ¹⁹ J. Rosén, A. Anders, S. Mráz, A. Atiser, J. M. Schneider, *J. Appl. Phys.* 99, 12303 (2006)
- ²⁰ A. Anders, G. Y. Yushkov, *J. Appl. Phys.* 91, 4824 (2002)
- ²¹ J.M. Schneider, A. Anders, B. Hjörvarsson, L. Hultman *Appl. Phys. Lett.*, 76, 12 (2000)
- ²² J. Rosén, A. Anders, S. Mráz, J. M. Schneider, *J. Appl. Phys.* 97, 10, 103306-1 (2005)
- ²³ J. Rosén, A. Anders, J. M. Schneider, *Appl. Phys. Lett.*, 80, 22, 4109 (2002)
- ²⁴ J. Rosén, A. Anders, J. M. Schneider, *Appl. Phys. Lett.* 89, 141502 (2006)
- ²⁵ A. Anders, *Cathodic Arcs*, Springer (New York, 2008) page 349

-
- ²⁶ Y. Y. Takamura, F. Koch, H. Maier, H. Bolt Surf.& Coat. Technol. 142-144, 260 (2001)
- ²⁷ G. Zosi, Thin Solid Films, 3, 13 (1969)
- ²⁸ W. C. Oliver, G. M. Pharr, J. Mater. Res., 7, 6, 1564 (1992)
- ²⁹ W.C. Oliver, G.M. Pharr J. Mater. Res., 7, 6, 1564 (1992)
- ³⁰ A. Schuetze, D. T. Quinto, Surf. Coat. Technol. **162**, 174 (2003)
- ³¹ G. Gutiérrez, A. Taga, B. Johansson Phys. Rev. B 65 012101 (2001)
- ³² J. M. Schneider, W. D. Sproul, R. W. J. Chia, M-S. Wong, A. Matthews, Surf.& Coat. Technol. 96, 262 (1997)

5.3 Influence of the substrate bias potential on the phase formation and elastic properties of Al_2O_3 films grown with cathodic arc

Alumina (Al_2O_3) films are used in application fields ranging from corrosion,¹ catalytic support,² diffusion barrier,³ and wear protection⁴ to microelectronics.⁵ Alumina is polymorphous and $\alpha\text{-Al}_2\text{O}_3$ is the thermodynamically stable phase. $\gamma\text{-Al}_2\text{O}_3$ becomes thermodynamically stable at small grain sizes due to its lower surface energy.⁶ Other metastable alumina phases include δ , η , θ , κ , β , and $\chi\text{-Al}_2\text{O}_3$.⁷ $\gamma\text{-Al}_2\text{O}_3$ was shown to sustain its structure at 1170°C during semi-solid processing of steel,⁸ which qualifies it as a candidate material for cutting tool protection, machining, and chipping applications.

The most established synthesis method of alumina films is CVD (Chemical Vapor Deposition),⁹ where the substrate temperature is typically well above 1000°C. Decreasing the substrate temperature has been a major goal for alumina (in particular $\alpha\text{-Al}_2\text{O}_3$) synthesis as most substrates undergo property changes at elevated temperatures. In order to do so, alternative routes were developed to deposit alumina phases. $\gamma\text{-Al}_2\text{O}_3$ thin films were deposited by plasma enhanced chemical vapor deposition at temperatures of 500 - 600°C.¹⁰ Chromia templates or initially oxidized CrN substrates were used to enable an $\alpha\text{-Al}_2\text{O}_3$ phase formation at lower temperatures such as 400°C¹¹ and 700°C¹², where Cr_2O_3 is acting as a seed layer for $\alpha\text{-Al}_2\text{O}_3$. Zywitzki et al. have used plasma activated electron beam evaporation for growing high quality dense $\gamma\text{-Al}_2\text{O}_3$ films at 700°C.¹³ Ionized magnetron sputtering was used to deposit low temperature crystalline alumina including $\kappa\text{-Al}_2\text{O}_3$ at temperatures as low as 320°C.¹⁴ Using cathodic arc deposition thin films containing $\gamma\text{-Al}_2\text{O}_3$ and $\alpha\text{-Al}_2\text{O}_3$ phases were deposited at temperatures as

low as 600°C.¹⁵ Recently, high power impulse magnetron sputtering was used to deposit films containing the γ -Al₂O₃ phase at 575°C.¹⁶

One of the most established strategies to decrease the substrate temperature is by applying a negative bias potential to the substrate. The additional energy delivered by ions accelerated across the substrate sheath may give results in an increased adatom mobility.^{17,18} In order to study the effect of the substrate bias potential on the phase formation, a monoenergetic singly charged discharge is employed. Earlier studies on the influence of a substrate bias potential on the phase formation and properties were carried out with discharges containing multiple charge states and/or energy distributions with high energy tails. Alternatively, the plasma composition and energy distribution functions were not reported. Hence, the discussion of the effect of the ion energy on the phase formation and properties was challenging due to presence of multiple charge states as well as broad energy distribution functions.

Here the effects of the ion energy on phase formation and elastic properties of alumina films deposited by cathodic arc method are reported. For the first time, an arc plasma containing only Al⁺, O⁺, O₂⁺ and Ar⁺ ions with narrow energy distribution functions are employed during growth.

The composition of the plasma as well as the ion energy distribution functions were measured with a mass-energy analyzer. No other charge states than 1+ could be identified for Al. Apart from Al⁺, also Ar⁺, O⁺ and O₂⁺ ions were present in the plasma. (Figure 5.3.1a) Further quantification, using the integrated ion energy distribution functions (IEDFs), resulted in the following plasma composition: 54.5% Ar⁺, 36.6% Al⁺, 4.2% O⁺, and 4.7% O₂⁺. (Figure 5.3.1b) The average energies of the ions were 10.6 eV for Al⁺, 8.5 eV for Ar⁺, 2.3 eV for O⁺, and 0.6 eV for O₂⁺.

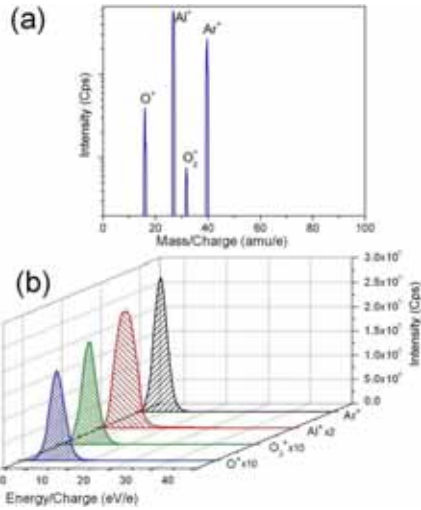


Figure 5.3.1: a) Composition of the plasma at 2 eV

b) IEDFs of Ar^+ , $Al^+ \times 2$, $O_2^+ \times 10$ and $O^+ \times 10$

The chemical composition of the films as measured by WDX is presented versus the substrate bias potential in Figure 5.3.2. The O/Al ratio was within 1 at.% deviation from the stoichiometric O/Al ratio of 1.5.

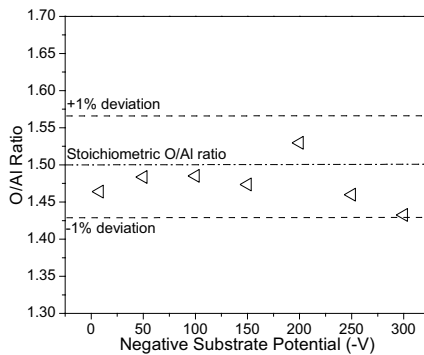


Figure 5.3.2: O/Al ratios as a function of the negative substrate bias potential

The sample grown at -300 V bias shows considerable delamination which is probably due to the build up of extensive compressive stress during deposition as a result of high energy bombardment of the surface and is therefore excluded from the discussion.

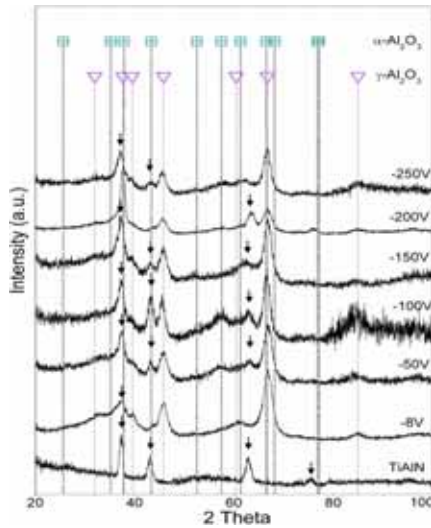


Figure 5.3.3: XRD data of films as a function of negative substrate bias potential

The structure investigations of the films were carried out by grazing incidence XRD (Figure 5.3.3). The XRD data of the TiAlN coated substrate prior to deposition is included as reference. The arrows indicate substrate related diffraction signals. There are four diffraction peaks visible for the TiAlN thin film at 2 θ values of 37.3, 43.0, 62.9, and 75.4 degrees. These values correspond to diffraction spots from 111, 200, 220, and 311 planes for cubic TiAlN.¹⁹ All other films presented comprise, in addition to the TiAlN based peaks, the γ -Al₂O₃ phase with the major peaks at 45.7° (400) and

66.7° (440) which represent the largest intensities according to JCPDS card: 10-425. There is no evidence for the presence of any other phase.

A direct comparison of this phase formation data with other reports in the literature is challenging because often growth relevant parameters such as arc current and voltage, filter shape and current, presence of additional magnetic fields, pressure and gas composition are not completely reported. We will however attempt to compare the here obtained data with Brill et al.¹⁵ and Rosén et al.¹⁷ Both reported the formation of the α -Al₂O₃ phase along with the γ -Al₂O₃ phase at 700°C substrate temperature and -200 V substrate bias potential. In the work of Brill et al., where α -Al₂O₃ is the dominant phase, the deposition rate is reported to be 0.2 nm/s, which is an order of magnitude lower than the deposition rate reported here (1.9 nm/s). Since kinetic factors may be important for the phase formation of Al₂O₃, the lower deposition rate may be important for the formation of the α -Al₂O₃ phase in the work of Brill et al.. Another significant difference in their work is the application of a RF bias potential in contrast to the pulsed DC bias potential applied here. Application of a RF bias may result in an increase in plasma density at the substrate. This may increase the number of metal and gaseous ions, affecting the plasma composition and hence the phase formation. Recently, it was shown that the presence of negative oxygen ions affects the structure evolution of transition metal oxide thin films.²⁰ Similarly, Rosén et al.¹⁷ have observed the formation of α -Al₂O₃ in a γ -Al₂O₃ matrix which was grown at a deposition rate of 1.0 nm/s, which is about half of the deposition rate reported in this work. This is consistent with the hypothesis presented above that α -Al₂O₃ is due to kinetic effects formed at low deposition rates.

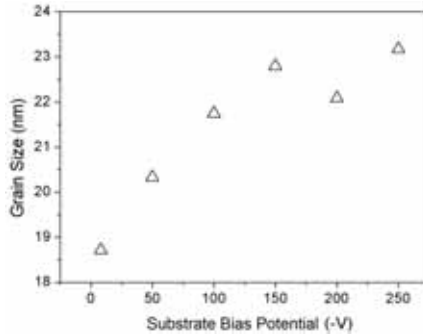


Figure 5.3.4: Grain size as a function of negative substrate bias potential

For the grain size estimation, the samples were measured with Bragg-Brentano geometry against a LaB_6 standard around the (400) peak. At this peak position there is no overlap with peaks from the TiAlN interlayer or from the $\alpha\text{-Al}_2\text{O}_3$ phase. The calculated grain size increases from 19 nm up to 23 nm as the substrate bias potential is increased from floating potential (-8 V) to -250 V (see Figure 5.3.4). It appears that the increase in the negative substrate bias potential does not influence the grain size significantly.

The elastic properties and topography measurements were carried out in an atomic force microscope based nanoindenter (Hysitron) equipped with a Berkovich diamond indenter with a tip radius of 100 nm. Reduced elastic modulus values were extracted from load-displacement curves and subsequently used for the calculation of the Young's modulus values according to the formula presented by Oliver and Pharr.²¹ In Figure 5.3.5, the Young's modulus values are presented as a function of the negative substrate bias potential. A sapphire sample was measured for reference and the resulting Young's Modulus agrees well with the Young's modulus value of $\alpha\text{-Al}_2\text{O}_3$ measured by Oliver and Pharr.²¹ The Young's modulus of $\gamma\text{-Al}_2\text{O}_3$ calculated

from bulk modulus values reported by ab-initio calculations²² and experimental measurements²³ (350 GPa) are included for comparison.

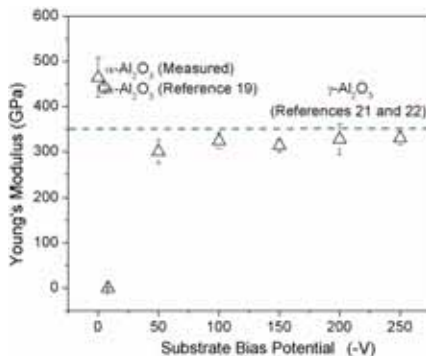


Figure 5.3.5: Young's Modulus values as a function of negative substrate bias potential

There is no significant change of the Young's modulus values measured for the substrate potentials from -50 V up to -250 V with a maximum deviation from literature values of 14% for the sample grown at -50 V and a minimum deviation from literature values of 5.7% for the sample grown at -250 V. The Young's modulus measured for the sample grown at -8 V was too low to be measured reliably. The reasons for this become apparent during the discussion of the film morphology.

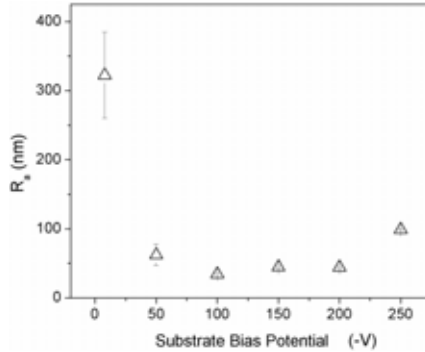


Figure 5.3.6: Surface roughness values as a function of negative substrate bias potential

Surface roughness values have been measured by atomic force microscopy (Figure 5.3.6). At negative substrate potentials from -50 to -250 V, the surface is relatively smooth exhibiting R_a values 34 to 99 nm. The sample grown at -8 V exhibits an R_a roughness value of 322 nm.

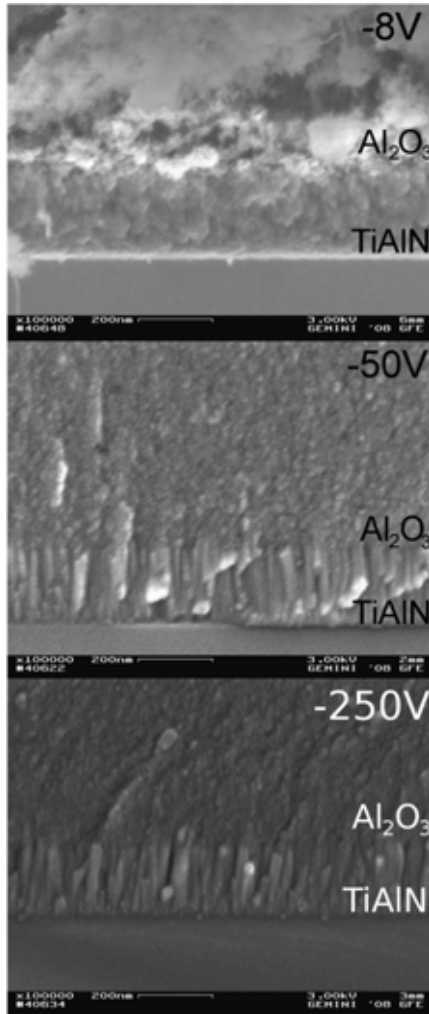


Figure 5.3.7: FESEM images for films grown at -8 V, -50 V and -250 V

In Figure 5.3.7, the FE-SEM cross section images of the films grown at -8 V, -50 V, and -250 V are presented. The film grown at -8 V is porous, which is consistent with the the very low Young's modulus and the large roughness values

presented earlier. The $\gamma\text{-Al}_2\text{O}_3$ film is $67.7\ \mu\text{m}$ thick, which corresponds to a deposition rate of $45.1\ \text{nm/s}$. The apparently high deposition rate is due to the undense film morphology. The sample grown at $-50\ \text{V}$ is dense. The thickness of the $\gamma\text{-Al}_2\text{O}_3$ film is about $1.9\ \mu\text{m}$, which corresponds to a deposition rate of $1.1\ \text{nm/s}$.

The film grown at $-250\ \text{V}$ is also dense. The $\gamma\text{-Al}_2\text{O}_3$ film is about $3.2\ \mu\text{m}$ thick corresponding to a deposition rate of $2.0\ \text{nm/s}$. The increase in deposition rate may be due to additional flux attracted to the substrate as the substrate bias potential is increased. A $180\text{-}200\ \text{nm}$ thick TiAlN film can be seen in all images.

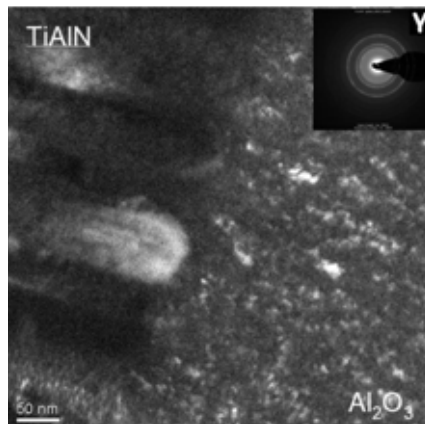


Figure 5.3.8: TEM and SAED image of the film grown at $-200\ \text{V}$ substrate bias potential (Repeated from Figure 5.2.7)

TEM and SAED diffraction were carried out for the film grown at $-200\ \text{V}$ substrate bias potential (Figure 5.3.8). The columnar structure of the TiAlN film and the equiaxed grained $\gamma\text{-Al}_2\text{O}_3$ are observed. Crystallites of about $20\ \text{nm}$ can be seen in different regions of the Al_2O_3 film. SAED diffraction analysis show that all diffraction

signals are consistent with the presence of $\gamma\text{-Al}_2\text{O}_3$. There is no evidence for the presence of another phase.

Annealing experiments were carried out in air for one hour at 800, 900, and 1000°C. The samples were introduced into the oven at room temperature, then heated at a rate of 10K/min and were subsequently cooled down at a rate below 10K/min. Differential scanning calorimetry was used to assess the thermal stability in an Ar atmosphere. The measurements were performed from room temperature up to 1500°C at a heating rate of 20 K/min.

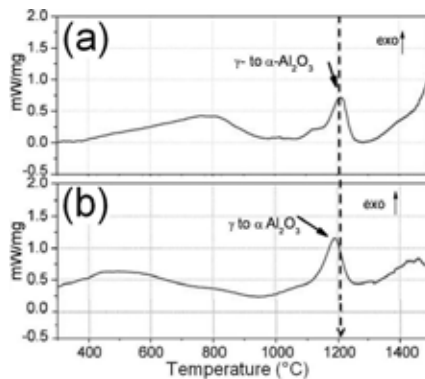


Figure 5.3.9: DSC measurements of a) the cathodic arc film grown at -200V substrate bias potential, and b) Commercial powder with particle size 150 μm

The DSC data compiled in Figure 5.3.9 of the cathodic arc film grown at -200 V bias potential (Figure 5.3.9a) was compared to commercial powder with a particle size of 150 μm and a domain size of 7,4 nm in Figure 5.3.9b. The maximum of the enthalpy signal indicating the γ to α phase transformation occurs at about 1200 °C for the thin film as well as the commercial powder. It appears that the γ to α

transformation of the thin films grown are very similar to the commercial $\gamma\text{-Al}_2\text{O}_3$ powder.

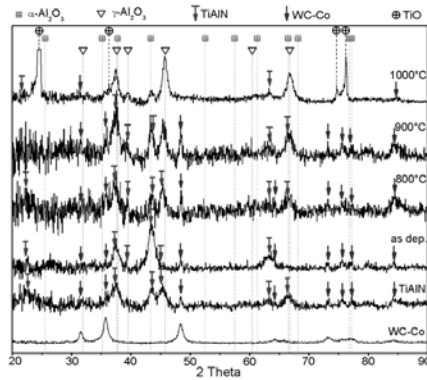


Figure 5.3.10: XRD data of the film deposited at -200V substrate bias potential as a function of the annealing temperature in air. The arrows indicate WC-Co (∇) and TiAlN (\triangle) related peaks.

In order to assess the chemical stability of the here produced $\gamma\text{-Al}_2\text{O}_3/\text{TiAlN}$ bilayers, annealing experiments were carried out in air. In Figure 5.3.10, XRD data of the film deposited at -200V bias potential is provided before and after annealing for one hour at 800°C, 900°C, and 1000°C. The diffractograms of the sample prior to annealing (as deposited), a hard metal substrate and a TiAlN coated hard metal substrate, are also included for reference, as before the substrate peaks are marked by arrows. At 800 and 900 °C, there are no new peaks visible, hence $\gamma\text{-Al}_2\text{O}_3$ appears to be stable at temperatures up to 900°C. It is well known that at 900°C spinodal decomposition of TiAlN occurs.^{24,25} At 1000°C the decomposition of TiAlN in fcc-TiN and fcc-AlN as well as hcp-AlN is commonly observed.^{24,25} The oxidation of AlN may serve as seed for the formation of $\alpha\text{-Al}_2\text{O}_3$ and thus facilitate the γ to α

transformation. Hence it is not surprising to observe substantial changes in the XRD diffractogram after annealing at 1000 °C. At this temperature, the dominant peaks are from the rutile (TiO₂) phase, suggesting that the decomposed TiAlN layer is oxidized by diffusive transport of oxygen through the γ -Al₂O₃ film. Also evidence for the formation of α -Al₂O₃ can be seen. Diffraction peaks at 2 θ angles of 35.2°, 52.6°, and 57.5° corresponding to the high intensity reflections of the (104), (024), and (116) planes of α -Al₂O₃ are visible. The presence of γ -Al₂O₃, α -Al₂O₃ peaks suggest an incomplete phase transformation. It is unclear at this point if the α -Al₂O₃ peaks stem solely from oxidation of the Al from the TiAlN or if the phase transformation from γ -Al₂O₃ into α -Al₂O₃ is initiated. However from a practical point of view, the application temperature of these films is limited to temperatures below 1000°C.

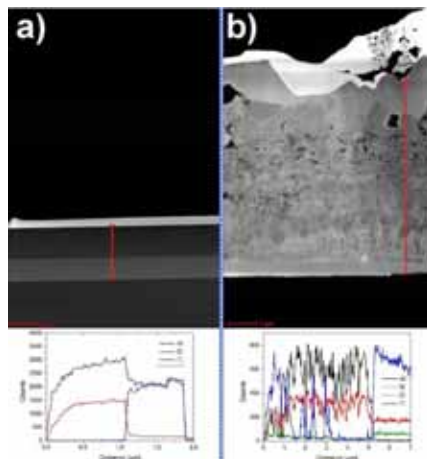


Figure 5.3.11: TEM images and associated line scans for a) TiAlN/Al₂O₃ film in as deposited state and b) TiAlN/Al₂O₃ film annealed for one hour in air at 1000°C.

In Figure 5.3.11a, the TEM image and the associated line scan are plotted for a TiAlN/Al₂O₃ bilayer in its as deposited state. The film is approximately 2 μm thick and there is a sharp boundary between the two bilayers at a distance of about 1 μm in the direction of measurement (see arrow). The oxygen signal goes to about zero, after this boundary, which means that the TiAlN film does not contain any significant amount of oxygen. Similarly, we do not see any Ti signal on the Al₂O₃ side of the bilayer. In Figure 5.3.11b, the TEM image and the associated line scan are plotted for a TiAlN/Al₂O₃ bilayer after it was annealed in air for one hour at 1000°C. The film is now approximately 7 μm thick and there is no sharp boundary between the bilayers. Furthermore the film appears porous and the oxygen signal is apparent throughout the film, indicating an oxygen diffusion from the surface to the substrate. The line scan is made unlike in the previous case, from bottom to top. On the surface, a thick TiO_xN_y layer is formed. It is conceivable that Ti reaches the surface by diffusion. The diffusion notion is supported by the presence of Ti at distances from 1.5 to 4 μm from the surface. It was already mentioned earlier that decomposition of TiAlN was expected at such high temperatures. As expected, we observe a low signal of N at the bottom of the film with respect to the top of the film. The remaining N indicates that some of Ti and Al close to the substrate is not yet oxidized. We also observe an overall increase of the film thickness, primarily due to the porous nature of the film. The porosity may stem from a number of reasons, one possible explanation is the volume change from γ to α transformation accompanied with N release from the TiAlN. The undense regions act as diffusion pathways, enabling a fast reaction of the TiAlN/Al₂O₃ bilayer. These findings suggest that both the stability of the interlayer and the morphology of the film (which determines to a large extent O₂ diffusion) are decisive for the phase stability of the γ-Al₂O₃/TiAlN films.

-
- ¹ V.A.C. Haanappel, H.D. van Corbach, T. Fransen, P.J. Gellings, *Surf. & Coat. Technol.* **72**, 13 (1995)
- ² C. R. Henry, *Surf. Sci. Rep.* **31**, 231 (1998)
- ³ J. Mueller, D. Neuschuetz, *Vacuum* **71**, 247 (2003)
- ⁴ D. Kurapov, J. Reiss, D. H. Trinh, L. Hultman, J. M. Schneider, *J. Vac. Sci. Technol. A* **25**, 4, 831 (2007)
- ⁵ S. Y. Wu, M. Hong, A. R. Kortan, J. Kwo, J. P. Mannaerts, W. C. Lee, Y. L. Huang, *App. Phys. Lett.* **87**, 091908 (2005)
- ⁶ J. M. McHale, A. Auroux, A. J. Perrotta, A. Navrotsky, *Science*, **277**, 788 (1997)
- ⁷ G. Paglia, A. L. Rohl, C. E. Buckley, J. D. Gale, *Physical Review B* **71**, 224115 (2005)
- ⁸ D. Kurapov, J.M. Schneider, *Steel Research Int.* **75**, 9, 577 (2004).
- ⁹ A.R. Barron, *Insulating materials: W.S. Rees Jr. (Ed.), CVD of Nonmetals*, VCH, Weinheim, 1996.
- ¹⁰ O. Kyrylov, D. Kurapov, J. M. Schneider, *Applied Physics A* **80**, 8, 1657 (2005)
- ¹¹ P. Jin, G. Xu, M. Tazawa, K. Yoshimura, D. Music, J. Alami, U. Helmersson, *J. Vac. Sci. Technol. A* **20** (6) (2002)
- ¹² T. Kohara, H. Tamagaki, Y Ikari, H. Fujii, *Surf. Coat. Technol.* **185**, 166 (2004)
- ¹³ O. Zywitzki, K. Goedicke, H. Morgner, *Surf. Coat. Technol.* **151-152**, 14 (2002)
- ¹⁴ J. M. Schneider, W. D. Sproul, A. Matthews, *Surf. Coat. Technol.* **98**, 1/3, 1473 (1998)
- ¹⁵ R. Brill, F. Koch, J. Mazurelle, D. Levchuk, M. Balden, Y. Yamada-Takamura, H. Maier, and H. Bolt, *Surf. Coat. Technol.* **174-175**, 606 (2003)
- ¹⁶ E. Wallin, T. I. Selinder, M. Elfving, U. Helmersson, *Europhys. Lett.* **82**, 36002 (2008)
- ¹⁷ J. Rosén, S. Mráz, U. Kreissig, D. Music, J. M. Schneider, *Plasma Chem. Plasma Process.* **25**, 4 (2005)
- ¹⁸ Y. Yamada-Takamura, F. Koch, H.Maier, H.Bolt, *Surf. Coat. Technol.* **142-144**, 260 (2001)
- ¹⁹ P. H. Mayrhofer, L. Hultmann, J. M. Schneider, P. Staron, H. Clemens, *Int. J. Mat. Res.* **98** 1054 (2007)
- ²⁰ S. Mráz, J. M. Schneider, *J. Appl. Phys.* **100**, 023503 (2006)
- ²¹ W. C. Oliver, G. M. Pharr, *J. Mater. Res.*, **7**, 6, 1564 (1992)
- ²² G. Gutiérrez, A. Taga, B. Johansson, *Phys. Rev. B* **65** 012101 (2001)
- ²³ A. Schuetze, D. T. Quinto, *Surf. Coat. Technol.* **162**, 174 (2003)
- ²⁴ A. Hörling, L. Hultman, M. Odén, J. Sjöln, L. Karlsson, *J. Vac. Sci. Technol. A* **20** 1815 (2002)
- ²⁵ P. Mayrhofer, D. Music, T. Reeswinkel, H. G. Fuß, J. M. Schneider, *Acta Mat.* **56**, 2469 (2008)

6. Conclusions and Future Work

In this chapter a summary of the results and discussions in this work will be presented. Some suggestions on future work will conclude the thesis.

6.1 Conclusions

The presence of high energy tails and higher charge states in cathodic arc plasmas made it challenging to study the influence of ion flux and energy on phase formation and thin film properties.

Charge state resolved Al ion energy distribution functions (IEDFs) were measured as a function of pressure distance product in the range from 0.01 to 256 Pa·cm. For the Al⁺ ion, a broad energy distribution with an average energy of 36.6 eV and an energy tail extending up to 110 eV was observed at 0.01 Pa·cm. As the pressure distance product was increased to 16 Pa·cm, the IEDF changed from a non-thermalized broad single ion population distribution into a double ion population distribution with a non-thermalized and a thermalized component. As the pressure distance product is increased further to 128 Pa·cm, the non-thermalized component disappears due to collisions and a narrow thermalized Al⁺ ion population distribution with an average energy of 2.6 eV (FWHM 2.1 eV) remains. The average charge state of Al is decreased from 1.58 to 1.0 as the pressure distance product was increased from 0.01 to 32 Pa·cm. Average energy and average charge state were shown to be affected by collisions, resulting in a monoenergetic beam of Al⁺ ions at p·d>128 Pa·cm.

The IEDFs were fitted by a single as well as a superposition of two shifted Maxwellian distributions and the fitting parameters are reported. The directional energies of both, the thermalized and non-thermalized metal ion populations, are decreased as the pressure distance product is increased due to collisions with the parent gas. For the same reason the random energy of the thermalized Al^+ population is decreased as the pressure distance product is increased. However, the random energy of the non-thermalized metal ion population is increased as the pressure distance product is increased due to the energy dependence of the scattering cross section, resulting in more efficient thermalization of ions with lower energy compared to the high energy fraction of the population.

The here presented plasma processing strategy resulting in a monoenergetic, single charged Al^+ plasma beam will enable growth experiments with controlled Al^+ ion energies. This is a prerequisite for studying the effect of ion energy on the phase formation without the effect of higher charge states and the presence of multiple populations in the IEDFs.

Subsequently, the plasma chemistry and energetics of an Al cathodic arc discharge was studied as a function of the filter current. Of the Al ions, only Al^+ was found, resulting in a charge state of 1.0 for all filter currents. The average energy of the Al^+ ions do not vary significantly, although a slight decrease from 1.4 to 0.3 eV is observed. At filter currents below 15 A, the plasma consisted predominantly of Al^+ ions (>94%) while at higher filter currents the populations of Ar and O ions increase. At 20 A, Al^+ constitutes only 36.3% of the plasma. The ion flux decreases an order of magnitude as filter current is increased from 10 to 20 A. The change in plasma composition and energetics may be due to a magnetic isolation of the anode which

would reduce the electron density near the source and increase it on the filter side. According to XRD and SAED data, the films grown at 10, 17, and 20 A are γ - Al_2O_3 . There is no evidence for the presence of another phase in these films. The films grown at 12 and 15 A contain a phase mixture of α - Al_2O_3 and γ - Al_2O_3 . The α - Al_2O_3 phase may have been formed due to additional energy that was delivered to the substrate via higher ion flux. A possible explanation for the unexpected loss in deposition rate at higher ion fluxes was presented suggesting that etching may be responsible. The grain size was calculated in the range from 20 to 30 nm via the Debye Scherrer method. TEM images have supported the grain size calculations. The elastic properties of the deposited films are reported. The average Young's modulus values of γ - Al_2O_3 films were 7-20% lower than calculated literature values. SEM and TEM investigations show that dense films can be grown with columnar as well as equiaxed grains.

To study the influence of substrate bias potential on phase formation and elastic properties of Al_2O_3 films grown with cathodic arc, a close to monoenergetic ion beam consisting of Al^+ , Ar^+ , and O^+/O_2^+ was employed for depositing Al_2O_3 thin films on TiAlN coated Si wafers as the substrate bias potential was varied from floating (-8 V) to -300 V. Wavelength dispersive x-ray spectroscopy measurements show an O/Al ratio of $1.5 \pm 1\%$ corresponding to the O/Al ratio of Al_2O_3 . XRD and SAED analysis indicate the presence of γ - Al_2O_3 in all films. No other phases were observed. The elastic properties were measured by nanoindentation. The Young's modulus values of the films grown within a substrate bias potential in the range of -50 to -250 V are no more than 14% smaller than the Young's modulus values obtained by ab initio calculations and nanoindentation experiments in the literature for γ - Al_2O_3 (350 GPa).

The cross sections of these films have been investigated by field emission scanning electron microscopy. It is found that the films grown from -50 to -250 V are dense. The γ -Al₂O₃ film deposited at -200V substrate bias potential is stable up to 1200°C in Ar atmosphere according to DSC data. The application temperature of γ -Al₂O₃ coated cutting inserts containing a TiAlN interlayer is limited to temperatures below 1000°C, based on our annealing experiments in air.

6.2 Future Work

It was shown that the ion flux and energy strongly affect the thin film properties, such as structure, density, Young's modulus, deposition rate, and surface roughness. It was also concluded that kinetics play an important role for all of the above mentioned properties.

Hence, the ion flux to the surface should systematically be varied. A flux reduction may be obtained by a pressure distance product increase, filter current optimization, and an increase of the scanning unit's coverage area. This may give some additional mobility to the adatoms, allowing them to move to energetically favorable positions, which may enable the formation of α -Al₂O₃ phase at lower temperatures.

Furthermore, it may be of interest to study the influence of the oxygen ion flux on phase formation and thin film properties. This may be achieved by introducing the oxygen within the filter as a function of distance to the cathode, or ionizing the oxygen within the chamber using an RF coil with an external RF generator. The latter

would change the plasma drastically and also make plasma diagnostics challenging, thus introducing the oxygen at different positions is the favorable approach.

Doping the cathode with Ti and Si, may affect the phase formation as well. This may be studied, together with theoretical methods, such as density functional theory, to enhance the stability of γ -Al₂O₃ thin films.

Resume

Name : Adil Atiser
Place/Date of Birth : Ankara, 15.01.1979
Nationality : Turkish

Educational Range of Experience

RWTH-Aachen University, Ph.D Student, May 2005 – December 2008

RWTH-Aachen University, Student Assistant, Oct 2003 – April 2005

Qualifications

Master of Science in Metallurgical Engineering Degree, April 2005, RWTH-Aachen

Graduation Thesis Title: Plasma Chemistry of RF Magnetron Sputtered Boron in Argon Atmosphere

Bachelor of Science in Metallurgical and Materials Engineering, January 2003, METU-Ankara

Graduation Thesis Title: Upgrade of the Quality System of an accredited NDT laboratory from EN 45001 to ISO/IEC 17025